8-2020

Evaluating the Hydraulic Performance of Digital Photogrammetry-Derived 3-Dimensional Models of a Hydraulic Structure Using Computational Fluid Dynamics

Tyler J. Ashby
Utah State University

EVALUATING THE HYDRAULIC PERFORMANCE OF DIGITAL PHOTOGRAMMETRY-DERIVED 3-DIMENSIONAL MODELS OF A HYDRAULIC STRUCTURE USING COMPUTATIONAL FLUID DYNAMICS

by

Tyler J. Ashby

A thesis submitted in partial fulfillment
of the requirements for the degree

of

MASTER OF SCIENCE

in

Civil and Environmental Engineering

Approved:

Steven L. Barfuss, M.S. Major Professor	Brian Crookston, Ph.D. Committee Member
Alfonso Torres-Rua, Ph.D. Committee Member	Richard S. Inouye, Ph.D. Vice Provost for Graduate Studies

UTAH STATE UNIVERSITY
Logan, Utah

2020

ABSTRACT

Evaluating the Hydraulic Performance of Digital Photogrammetry-Derived 3-Dimensional Models of a Hydraulic Structure Using Computational Fluid Dynamics

by

Tyler J. Ashby, Master of Science

Utah State University, 2020

Major Professor: Professor Steven L. Barfuss
Department: Civil and Environmental Engineering

This research investigated the combination of aerial imagery, photogrammetry, and computational fluid dynamics (CFD). Aerial imagery of an 8-ft ramp flume in an unlined canal was collected using a DJI Mavic 2 Pro UAV. The aerial imagery was processed using a commercial photogrammetry software. Two 3D models were developed from the aerial imagery using a commercial photogrammetry software. One model was developed using ground control points (GCP) to improve and measure the accuracy of the model. The other model used the GCPs as check points, which only measured the model's accuracy. These two models are referred to as the GCP model and the Non-GCP model, respectively.

The GCP model and Non-GCP models' spatial accuracy was assessed. The horizontal and vertical root mean square errors (RMSE) were, respectively, 0.39 in. and 0.73 in. for the GCP, and 59.60 in. and 661.96 in. for the Non-GCP model. The Non-GCP model was shifted by 56.35 in. (northing), -12.52 in. (easting), and -662.22 in. (vertical)

to remove bias, which resulted in precision horizontal and vertical RMSE of 5.37 in. and 2.80 in., respectively.

In addition to the GCP and Non-GCP models, two hybrid 3D models were also developed for CFD testing. The first hybrid 3D model was developed by replacing the GCP model's flume with a CAD-modeled version of the flume from the original design. The second hybrid 3D model was developed using physically-measured dimensions of the flume. These two hybrid models are referred to as the As-Designed and As-Built models, respectively.

All four 3D models were numerically modeled at four flowrates each: 10.0 cfs, 23.0 cfs, 39.7 cfs, and 50.0 cfs. The middle flowrates correspond to observed flowrates during site visits. The outer flowrates correspond to flowrates at extreme ends of expected operating conditions. The differences in water depth at the stilling well location for each model at 10.0 cfs, 23.0 cfs, 39.7 cfs, and 50 cfs was, respectively:

- GCP: 0.045 ft (8%), 0.015 ft (2%), -0.024 ft (-2%), and -0.053 ft (-4%)
- Non-GCP: 0.055 ft (9 %), -0.007 ft (-1%), -0.024 ft (-2%), -0.025 ft, (-2%)
- As-Designed: 0.081 ft (13%), 0.059 (6%), 0.011 ft (1%), 0.006 ft (0%)
- As-Built: 0.047 ft (8%), 0.068 ft (7%), 0.026 ft (2%), and 0.031 ft (2%)

The CFD results indicated that photogrammetry can be used to develop hydraulically-accurate 3D models if GCPs are used.

(66 pages)

PUBLIC ABSTRACT

Evaluating the Hydraulic Performance of Digital Photogrammetry-Derived 3-Dimensional Models of a Hydraulic Structure Using Computational Fluid Dynamics

Tyler J. Ashby

This research investigated the combination of aerial imagery, photogrammetry, and computational fluid dynamics (CFD). Two 3D models of an 8-ft ramp flume were developed from aerial imagery using a commercial photogrammetry software. The GCP model was developed using ground control points (GCP) to improve and measure the model's accuracy. The Non-GCP model used GCPs as check points, which only measure the model's accuracy. The horizontal and vertical errors were, respectively, 0.39 in. and 0.73 in. for the GCP model, and 5.37 in. and 2.80 in. for the Non-GCP model.

In addition to the GCP and Non-GCP models, two hybrid 3D models were also developed for CFD testing. The As-Designed model was developed by replacing the GCP model's flume with a CAD-modeled version of the flume from the original design. The As-Built model was developed using physically-measured dimensions of the flume.

All four 3D models were numerically modeled at four flowrates: 10.0 cfs, 23.0 cfs, 39.7 cfs, and 50.0 cfs. The differences in water depth at the stilling well ranged between -4% and 8% for the GCP model, -2% and 9% for the Non-GCP model, 0% and 13% for the As-Designed model, and 2% and 8% for the As-Built model. The CFD results indicated that photogrammetry can develop hydraulically-accurate 3D models.

ACKNOWLEDGMENTS

I would like to thank my dear wife, Victoria Ashby, for her support, encouragement, and patience she continuously offers. She has been instrumental in my perseverance, and I couldn't have made it to this point without her help. I am also extremely grateful for the guidance, counsel, and assistance from my major professor, Professor Steve Barfuss. I also express my appreciation to my other committee members, Dr. Alfonso Torres-Rua and Dr. Brian Crookston for their sound advice and assistance.

There is a long list of other individuals who have offered meaningful contributions throughout the process. Several other professors provided selfless assistance and shared their excitement for my research including Drs. Zac Sharp, Mike Johnson, Wade Goodridge, Blake Tullis, Bethany Neilson, and Professor Austin Ball. Mark Winkelaar provided invaluable assistance managing the geospatial data from the research. Several professionals including Richard Boudrero, Jason Morgado, Keith Meikle, and Paul Willardson were extremely facilitating and quickly replied to all of my queries. Finally, I would be remiss if I didn't thank my parents, my siblings, and my friends that supported me and showed interest in my research. The list could go on, and if I omitted any individual, it is not intentional; I have been very blessed by the vast amount of support I've received. Thank you all.

Tyler J. Ashby

CONTENTS

Page

LIST OF FIGURES

Figure Page

LIST OF TABLES

CHAPTER I

INTRODUCTION

Water is commonly referred to as one of the world's most precious resources. As such, it is essential to monitor how and where water is distributed. One common means for measuring flowrates in an open channel is a hydraulic structure. Open channel hydraulic structures may include dams, weirs and flumes. These structures cause a predictable and measurable change to flow characteristics so engineers can measure or predict the flowrate associated with those specific flow characteristics.

Open-channel flow measurement structures and control structures are essential components to water management infrastructure. The United States' infrastructure is in poor condition, as indicated by the American Society of Civil Engineers' (ASCE) most recent infrastructure report card (2018). The dam and levee sections each received a D grade, which denotes that the infrastructure is "at risk".

In ASCE's 2015 report (2016) for the state of Utah, the state's dams, levees, and canals earned grades of B-, D-, and D+, respectively. A B grade indicates that the infrastructure is "adequate for now." The Utah report card also discusses that the canals in Utah "exist without any regulatory programs…, predate modern construction (over 100-years in age) …, [and] are largely self-regulated by approximately 1,400 canal companies which are operated with diminishing funding and resources."

ASCE's assessment of the current state of water management infrastructure in the nation and state demonstrates the need to more closely monitor and assess important structures. The safety of dams and levees may be improved, and the efficiency of canals increased by properly monitoring the hydraulic structure's condition as well as modeling

their performance within these systems.

Purpose

The research presented in this thesis focuses on using aerial imagery as a means to develop numerical models of hydraulic structures. Aerial imagery is processed using digital photogrammetry software to develop 3D models of hydraulic structures that can then be analyzed using computational fluid dynamics (CFD). Photogrammetry is the science of obtaining spatial information from photographic imagery (Aber et al. 2010). CFD is a numerical modeling method commonly used to simulate fluid flow. In hydraulics, it can be used as an analytical tool to predict or evaluate flow characteristics of closed conduits or open-channel systems.

It is not uncommon to use light detection and ranging (lidar) to develop 3D models of hydraulic structures that can then be used for a wide variety of applications, including monitoring structures and CFD analyses. However, there is a significant cost difference between visible-light imagery sensors and lidar sensors. Visible-light imagery is simply a photograph that captures the wavelengths of light that are naturally visible to the human eye. Torres (2019) pointed out that quality lidar sensors cost at least $50,000, and a full lidar system may cost between $150,000 and $300,000.

The systems and software associated with this research cost approximately $1600 for the unmanned aerial system (UAS) and $500 for the educational version of the photogrammetry software. An UAS is a comprehensive system that includes an unmanned aerial vehicle (UAV), ground control station, communications link, and payload. Therefore, this research sheds valuable light on the potential use of relatively low-cost UASs to develop useful and valid 3D models and CFD simulations.

Although 1D and 2D numerical modeling is more common for rivers and other open channels, a 2D CFD model would not be likely to properly represent the inherently 3D flow conditions at a hydraulic structure. Therefore, 3D CFD is used to more accurately capture the flow characteristics at a control structure, which realistically include major flow components in all three dimensions.

The structure studied in this research is an 8-ft wide concrete long-throat ramp flume in the Logan, Hyde Park, Smithfield (LHPS) Canal at approximately 41° 48' 51.82" Latitude, 111° 48' 9.65". The flume is installed in an unlined earthen canal. The flume was selected due to its proximity to Utah State University, ease of access, little vegetation taller than turf, and because the canal is drained during non-irrigation season. These conditions accommodate capturing usable imagery to develop the 3D models.

Rendering a hydraulic structure using low-cost photography could certainly allow engineers to monitor the physical condition of hydraulic structures. However, the research in this thesis focuses on the accuracy of the rendered hydraulic structure geometry using 3D photogrammetry within fluid flow CFD simulations. The CFD analysis presented in this research includes simulations for four model variations of the LHPS flume. The four models are developed from the same aerial imagery, but the use of ground control points (GCP), As-Built dimensions, and design dimensions varies among the models. The CFD analysis is a means to identify how each model compares to the structure's current rating curve, which was theoretically established within WinFlume. This data provides a means to quantify the hydraulic accuracy of the 3D models, whereas the literature to date almost exclusively focuses on spatial accuracy of digital photogrammetry.

CHAPTER II

LITERATURE REVIEW

This chapter briefly reviews previous research that investigates the use of UASs in water resources and structure modeling. Literature regarding CFD modeling of hydraulic structures is also reviewed.

The first academic application of an UAS is attributed to Przybilla and Wester-Ebbinghaus (1979). Przybilla and Wester-Ebbinghaus developed a radio-controlled fixed-wing aircraft with a camera as its payload. Their research investigated using an UAV to acquire close-range imagery to be used for photogrammetry. Although the value of such applications of data from UAVs wasn't immediately recognized, academic research involving UAVs has greatly increased over the past 20 years.

For example, Colomina and Molina (2014) pointed out that the International Society for Photogrammetry and Remote Sensing (ISPRS) congress saw an increase from 3 papers related to UAVs in 2004, to 21 papers in 2008, and 50 in 2012. There are many research applications for UAVs besides photogrammetry and remote sensing, but these statistics effectively indicate the increased use and application of UAVs across the world.

Practical applications of UAV imagery and data vary widely and include topics relevant to water resources such as agricultural efficiency (Chao et al. 2009), structural integrity of dams (Henriques and Roque 2015), and hydromorphology (Woodget et al. 2017). Each of these applications can have a meaningful impact on water use in society. The branch of UAV research that most closely relates to the research presented in this thesis is remote sensing for hydrologic and hydraulic modeling.

Reali (2018) used UAVs to expand efforts to use satellite remote sensing data by

Casas et al. (2006) and Schumann et al. (2008) to develop 1D hydraulic models from DEMs of entire flood plains and river basins. Similarly, King et al. (2018) and Yang et al. (2019) sought to estimate discharge and attenuation, respectively, of ungauged rivers. Each of these studies relies on the assumption that flow is effectively 1D, which at such a large scale appears to be both practical and reasonable. The author could find no previous research investigating 3D numerical models of hydraulic structures that originated from aerial imagery and photogrammetry.

However, hydraulic structures are continuously modeled using 3D CFD where the structure geometry was developed using computer-aided design (CAD) to model a given set of dimensions. The channel the structure is modeled in is either idealized as flat and planar, or scanned in some way to capture actual conditions. Scanning methods commonly include lidar and sonar.

Willeitner et al. (2013) implemented CFD to develop correction factors for various sizes of submerged Montana flumes. The Montana flumes were modeled using the standard dimensions of Parshall flumes without a diverging section downstream of the throat. Zeng et al. (2018) also performed numerical modeling on hydraulic structures using only CAD programs to develop the 3D models. No attempt was made to gather bathymetric data for the river they studied in their research, and they modeled the weirs and ship locks in CAD as well.

Some modeling has been performed on hybrid models that include a CAD-modeled hydraulic structure integrated into some type of 3D scanned model of a channel. Loor et al. (2018) combined a bathymetry model of a river bed and CFD to investigate flow conditions at a damaged weir. The bathymetry data originated from a 5 m resolution

dataset called Baseline. The author was unable to find the method by which the Baseline bathymetry data was collected. Similarly, Cook et al. (2002) used bathymetry data and engineering drawings to develop CFD tests of a spillway, stilling basin, and tailrace downstream of a dam. Again, no detailed information regarding the method of collecting bathymetric data was included in their paper. Chen et al. (2019) even used photogrammetry to model several mountain streams to quantify flow resistance. Their study, however, did not include any hydraulic structures within the streams they modeled. Even though several CFD studies have been performed using various methods to develop surface geometry of the channel bed, there does not appear to be any previous literature that uses photogrammetry to develop a working model of both the channel bed and hydraulic structure.

CHAPTER III

DATA COLLECTION

The data collected for and used in this research consists of aerial imagery, GCP locations, and flume dimensions. There were four different methods used to model the flume's geometry, and each method corresponds to its own model used in the subsequent CFD analysis. The four methods used to model the flume's geometry are:

- Photogrammetry results associated with using nine of the GCPs as accuracy control points. This model is hereafter referred to as the GCP model.
- Photogrammetry results associated with not using GCPs as accuracy control points. This model is hereafter referred to as the Non-GCP model.
- Original design dimensions for the flume. This model is hereafter referred to as the As-Designed model.
- Physically-measured dimensions for the flume. This model is hereafter referred to as the As-Built model.

The aerial imagery and GCP locations are applied universally to all four models of the flume. This chapter summarizes the methods used to collect the aerial imagery, GCP locations, and the four variations of the flume's geometry.

Aerial Imagery

The UAV the author used to gather the aerial imagery for this research is the DJI Mavic 2 Pro. The Mavic 2 Pro has an integrated L1D-20c model Hasselblad camera with and RGB lens, a 77° field of view, and a resolution of 5472 x 3648 pixels (20

megapixels). The UAV also features a GPS system which allows the UAV to record its geographic location as each image is captured.

The author used a flight planning software, Litchi, to program the flights. The Litchi software on the GCS mobile device was version 4.16.0. In order to capture sufficient detail and area, seven flight paths were planned at four different elevations. Two flight paths were planned at 15 ft, 40 ft, and 70 ft above ground level, and one was planned at 120 ft above ground level. The two flights at each of the lower altitudes corresponded to the type of imagery that path was intended to capture, either nadir or oblique. Nadir imagery is taken with the camera pointed directly toward the ground. Oblique imagery is taken at an angle between vertical and horizontal. Figure 1 shows the flight paths planned using Litchi, where purple markers are waypoints and blue markers are focus points. Figure 2 shows an example of nadir imagery and oblique imagery.

(a) (b) (c)

Figure 1. Planned flight paths: (a) nadir imagery path for 120 ft flight; (b) oblique imagery path for 15, 40, and 70 ft flights; (c) nadir imagery path for 15, 40, and 70 ft flights

(a) (b)

Figure 2. (a) Nadir image of LHPS flume, (b) oblique image of LHPS flume

Imagery was taken during three different flights. Since the author only had one battery, which generally lasts between 20 and 30 minutes of flight, the three flights were not consecutive. Two flights occurred on November 9, 2019 and one flight occurred on November 12, 2019. The first flight began on November 9 at 10:51 am and ended at 11:11 am, and the second flight began at 1:31 pm and ended at 1:48 pm. The third and final flight began on November 12 at 10:43 am and ended at 10:59 am. Taking imagery of the same location at different times or on different days is not recommended, since there can be significant lighting changes that can hamper the photogrammetry results. However, it appears that the lighting was similar enough across the three flights' images that the photogrammetry results were not significantly impacted by the slight differences in shadows.

The camera was placed on automatic exposure mode, so some photographic parameters vary from image to image. It is important to note that, for imagery intended to be used in photogrammetry, these settings are usually manually set to prevent inconsistencies between overlapping photos. The author was unaware of this process at the time the imagery was taken. Therefore, the shutter speed, aperture, and focal distance

vary among the images. Table 1 shows the number of images taken during all three flights at different settings associated with automatic exposure mode. In addition to the settings that varied due to the automatic exposure mode, ISO was 100 and exposure compensation (EV) was 0 for all images.

Table 1. Numbers of photos taken at various shutter speeds, apertures, and focal lengths

Shutter Speed		**Aperture**		**Focal Length**	
# Photos	(s)	# Photos	f-	# Photos	(m)
2	1/640	191	5.0	22	1.52
121	1/500	498	5.6	498	1.71
183	1/400	22	6.3	191	1.91
371	1/320				
31	1/240				
3	1/200				

Ground Control Points

The GCPs were marked by numbered aerial targets printed on 8 1/2" x 11" paper. Figure 3 shows the pattern of the GCPs. Consistent with recommendations from literature, the author placed GCPs throughout the study area (Smith and Vericat 2015) with an approximate spacing of 40 ft between GCPs (Ridolfi et al. 2017) at like elevations. Twelve total GCPs were placed in the study area; four were placed inside the canal, three were placed on each bank, and one was placed on the stilling well structure adjacent to the flume. Figure 4 shows the location of the GCPs within the study area.

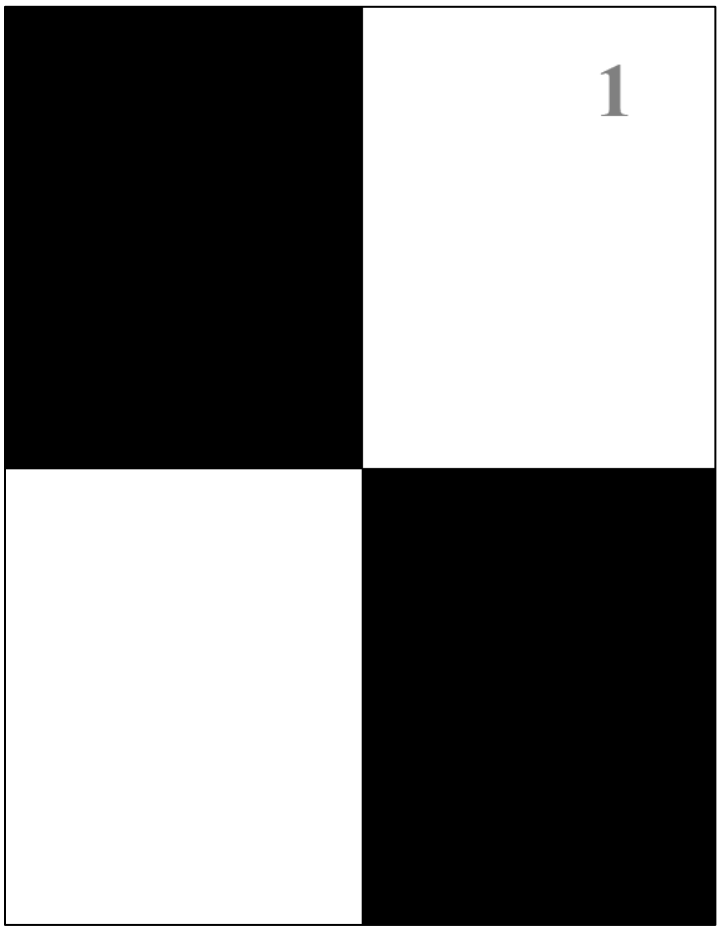

Figure 3. Ground control point marker pattern

Once the GCPs were placed, the geographic location and elevation of each was measured using a real-time kinetic global positioning system (RTK-GPS). RTK systems have two main components: a base station GPS receiver and a rover GPS receiver. The base station must remain in place for a long period of time, typically at least 8 hours, to establish a highly accurate geographic location for itself. The rover then measures its position relative to the base station with a high degree of accuracy, usually under 1 in. horizontally and 2 in. vertically.

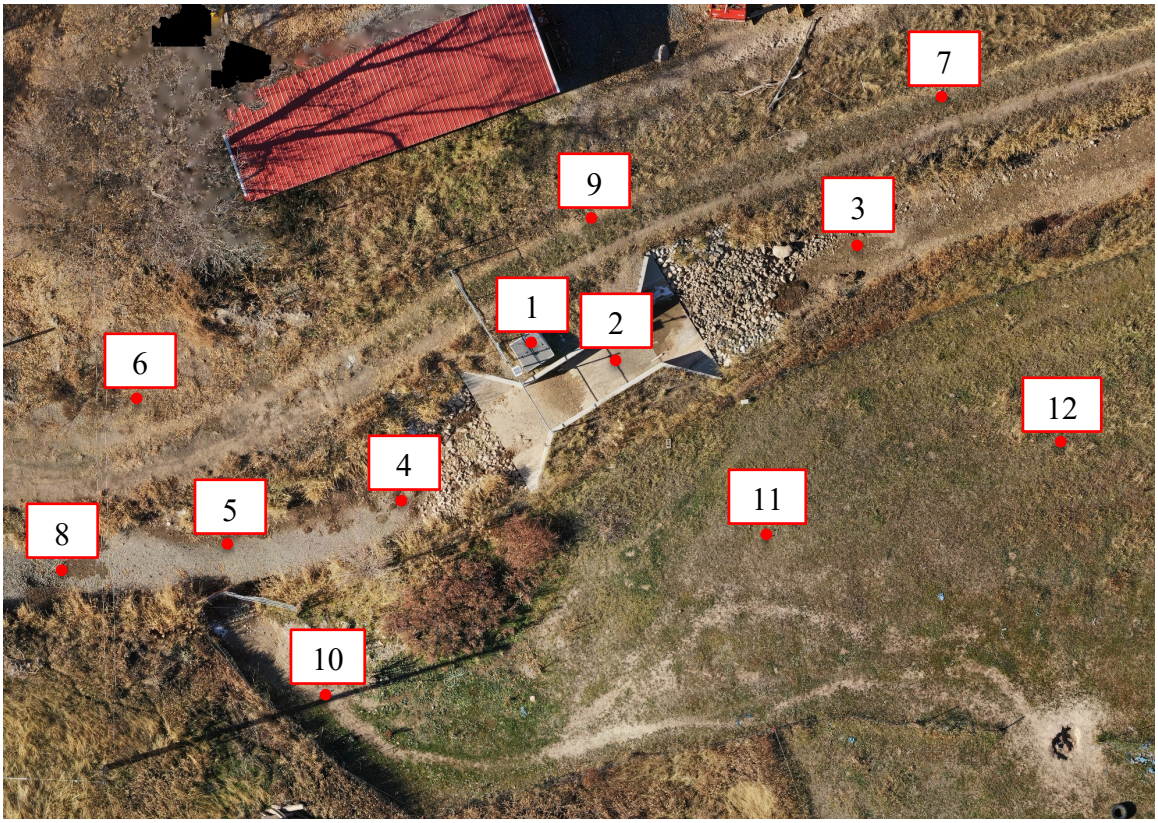

Figure 4. Orthophoto of study area showing the location of the GCPs

The base station of the RTK system used for this research is a permanent fixture operated and maintained by Logan City. The rover system consisted of a Trimble R6 GNSS receiver and a Trimble TSC2 data collector. The GCP locations were recorded by the rover in the North America Datum of 1983 (NAD83) Utah North Survey Feet projection system and the North American Vertical Datum of 1988 (NAVD88). The rover was held in place by a tribrach and recorded the location of each GCP for at least five minutes.

GCP Model Flume Geometry

The flume geometry for the GCP model was developed during the photogrammetry phase of this research. The photogrammetry phase also modeled the

channel bed and its features. The GCP model features the use of nine of the twelve GCPs as accuracy control points. Accuracy control points constrain the model geometry to more accurately represent the actual physical geometry of the site. The other three GCPs were used as check points. Check points are not used to develop the model but only measure the accuracy of the model once it is developed. Chapter IV discusses the workflow of the photogrammetry phase, and Chapter V addresses the spatial accuracy.

Non-GCP Model Flume Geometry

The flume geometry for the Non-GCP model was also developed using photogrammetry. However, none of the GCPs were used as accuracy control points. Instead, all 12 GCPs were used as check points. While it is well understood that a lack of GCPs in photogrammetry leads to a spatially inaccurate model, this model was developed to investigate the hydraulic effects of the spatial inaccuracies associated with not using GCPs. Further details about the development and spatial accuracy of the Non-GCP flume are also presented in Chapters IV and V, respectively.

As-Designed Model Flume Geometry

The design dimensions of the flume were extracted from the design drawings produced by J-U-B Engineers, which are shown in Figures A1 and A2 (J-U-B Engineers 2014). It is important to note that the original sill height was listed as 1 ft 1 in. but was later changed to 6 in.

The As-Designed model was included in the research to include a model more similar to those used by Loor et al. (2018) and Cook et al. (2002), where the channel geometry was modeled using some type of 3D scanning technique, but the hydraulic

structure was developed within a CAD software. The comparison between methods of modeling the hydraulic structure's geometry may provide valuable insight into the accuracy and relative differences between the methods.

As-Built Model Flume Geometry

The actual, or As-Built, dimensions of the flume were collected using a 25 ft tape measure with a precision of 1/16 in. The floor, incline, sill, decline, and wingwalls were all assumed to be flat, and the floor and sill were assumed to be level. Figures A3 and A4 show the measured dimensions of the flume.

Similar to the As-Designed model, the As-Built model was included to more closely resemble former work related to this research. Most large hydraulic structures are measured after construction, and the new measurements may be used instead of the design drawings in a numerical model.

CHAPTER IV

PHOTOGRAMMETRY AND 3D MODEL DEVELOPMENT

A total of four models of the LHPS flume were developed for this research. The GCP model was developed within the digital photogrammetry software, Agisoft Metashape version 1.6.1, using nine of the GCPs as accuracy control points and three of the GCPs as check points. Agisoft Metashape will be referred to subsequently as Agisoft. The GCPs used as check points provide a means to quantify the accuracy of the output model. The Non-GCP model was also developed within Agisoft. All GCPs were only used as check points, which means that no GCPs contributed to the model's accuracy. Two more hybrid models were developed using the GCP model as a base model by digitally removing the flume from the GCP model and replacing it with a flume model created within Autodesk Inventor Professional 2020.0.0. The As-Designed and As-Built flume models created within Inventor correspond to the design dimensions (Figures A1 and A2) and the physically-measured dimensions (Figures A3 and A4), respectively.

This chapter summarizes workflow and parameter settings used within Agisoft to develop the GCP and Non-GCP models. The process of replacing the flume in the GCP model with the As-Designed and As-Built flumes is also briefly discussed.

GCP Model Development

Digital photogrammetry is the method by which the 3D GCP model was developed from the aerial images. This section includes a brief discussion of the workflow and parameter settings used within Agisoft.

The first step in the Agisoft workflow is importing the photos and GCPs. All valid images from all three flights were imported. Some images were mistakenly taken of

subjects not within the study area. Such images were excluded from import. The image coordinates were then converted to match the GCP system of NAD83 and NAVD88. The images were also filtered to remove images with an image quality lower than 0.7. The photos were then aligned according to the parameters shown in Figure 5.

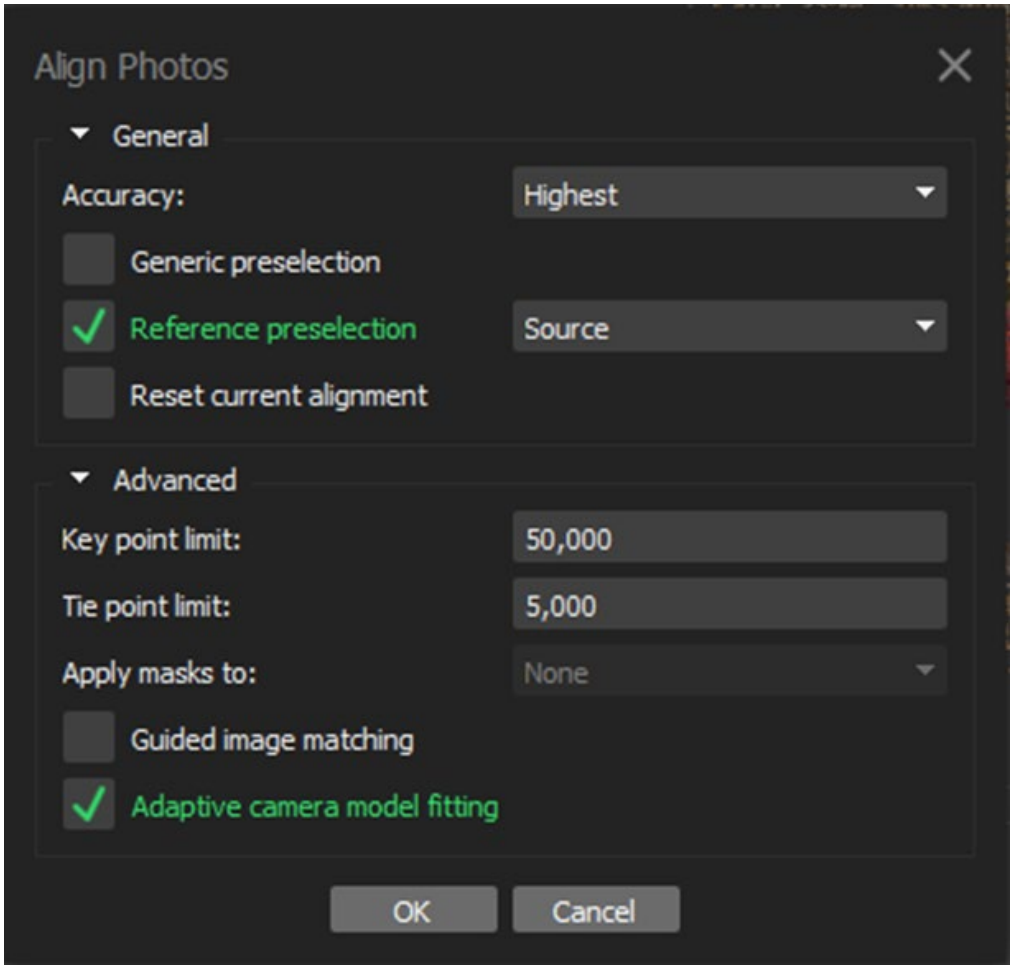

Figure 5. Photo alignment parameters within Agisoft Metashape

A sparse point cloud is generated from the image alignment process. The sparse point clouds used in this research were refined by removing points with a reprojection error above 0.7 or a reprojection uncertainty above 65. The GCPs were manually marked in at least 20 images per GCP. After marking the GCPs, the camera alignment was optimized with the “Adaptive camera model fitting” option selected. GCPs 5, 9, and 11

were unchecked during camera alignment optimization for the GCP model. This means that Agisoft used the other nine GCPs as accuracy control points, while the three unchecked GCPs were only used as check points. After refining the sparse point cloud, marking the GCPs, setting check points and control points, and optimizing the camera alignment, a dense point cloud was generated using the parameters shown in Figure 6.

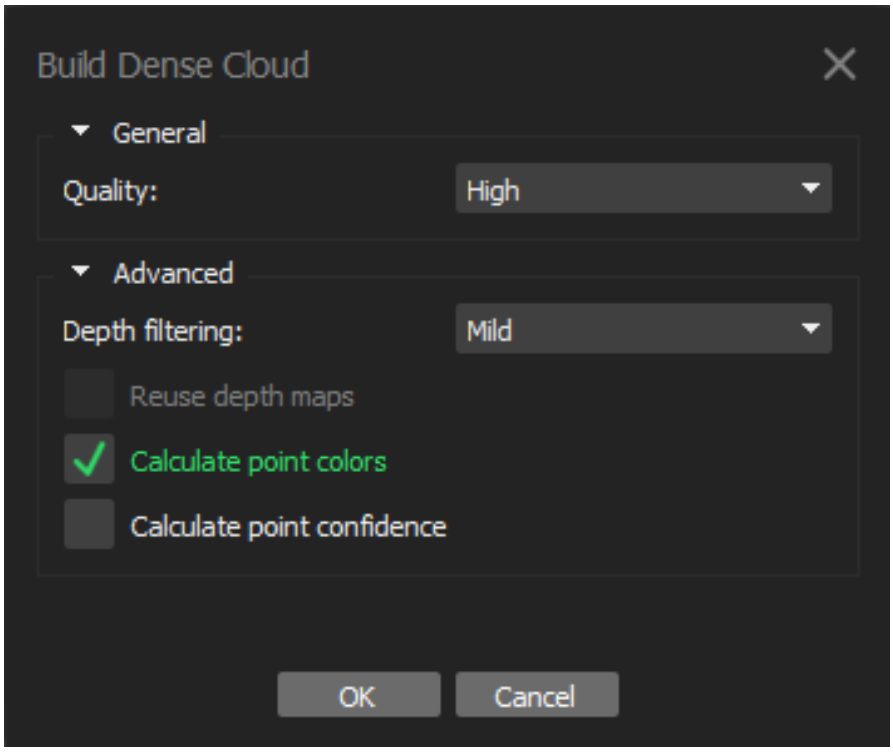

Figure 6. Dense point cloud creation parameters within Agisoft Metashape

Once the dense point cloud was generated, areas of the point cloud well outside of the area enclosed by GCPs were manually trimmed. A mesh was then generated using the parameters shown in Figure 7.

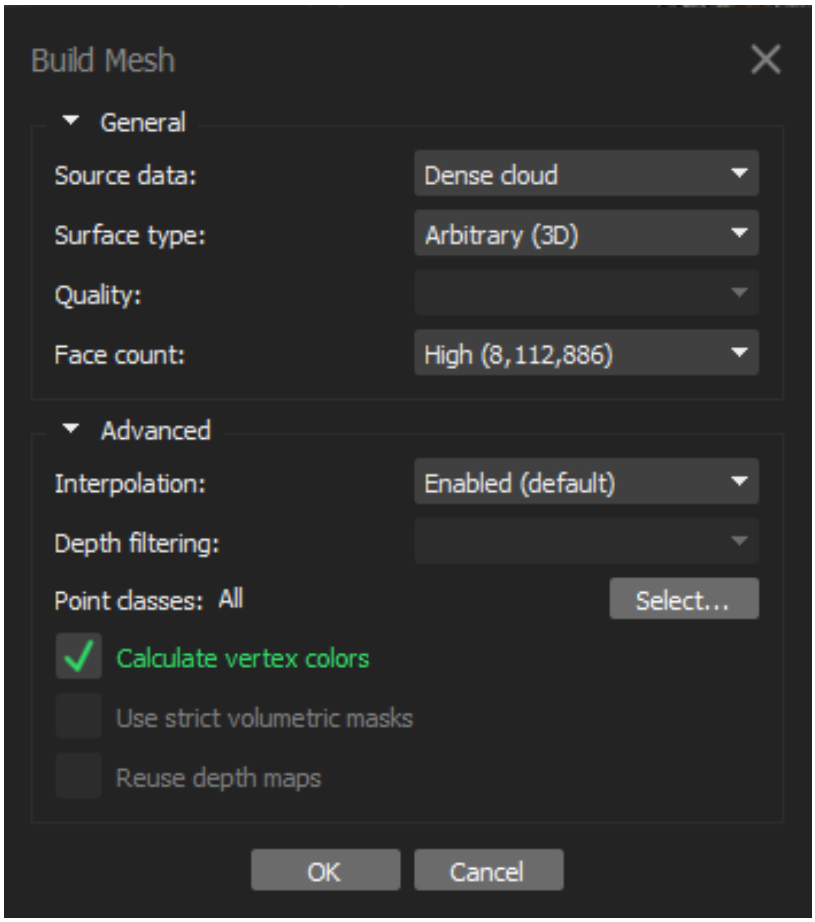

Figure 7. Mesh creation parameters within Agisoft Metashape

The mesh resulting from this operation was highly complex and had many self-intersecting faces, likely due to the image resolution. Several operations were carried out within Agisoft to simplify and refine the surface mesh in Agisoft. First, further manual trimming reduced the mesh to just the canal area. Then the mesh was decimated from just over 8 million faces to 2 million faces. This resolved most of the issues within the bed of the channel. The vegetation along the sides of the canal was still very complex, so the sides were manually selected and passed through a smooth mesh operation with strength of 35, then again with a strength of 30.

It is important to note that the resulting representation of the vegetation was a

surface which would effectively be a wall within the CFD simulations. This is a notable difference compared to the real physical condition in which water would be able to flow through and around the vegetation along the banks. The digital and numerical representation could be an oversimplification of the vegetation problem, but this topic is not within the scope of this research. After refining the mesh as described, it was exported as a stereolithography (.stl) file, which is an importable file type for the CFD software used in this research, STAR-CCM+.

Non-GCP Model Development

The workflow and parameters used to develop the GCP model are nearly identical to those used to develop the Non-GCP model. The greatest difference between the GCP and Non-GCP model is the application of GCPs. The Non-GCP model implements all GCPs as check points. Since no accuracy control points are established, the geometry is developed using only the relative spatial data Agisoft gathers from the overlapping imagery. Besides the use of GCPs, all other steps carefully replicated those used to develop the GCP model.

As-Designed Model Development

Once the As-Designed flume was created in Inventor, the GCP model and the As-Designed flume were imported into STAR-CCM+ to integrate the flume into the GCP model. The flume portion of the GCP model was removed using a subtractive Boolean operation, and the As-Designed model was then united with the remaining channel bed.

As-Built Model Development

Similar to the As-Designed model, the As-Built flume was first created in

Inventor. The GCP model and As-Built flume were then imported into STAR-CCM+. The flume portion of the GCP model was removed, and the As-Built model was united with the GCP model's channel bed.

CHAPTER V

PHOTOGRAMMETRY RESULTS AND DISCUSSION

There are two primary outputs from the photogrammetry and CFD modeling that provide a quantitative means to evaluate the accuracy of the models used in this research. The photogrammetry output is the offset between the modeled location and the actual location of the GCPs. The CFD output is the piezometric head (h_p) measured for a specific flowrate at the stilling well location. This chapter focuses exclusively on the photogrammetry output. Since the As-Designed and As-Built models use the GCP model as a basis, neither is discussed in this chapter.

GCP Model Photogrammetry Results and Discussion

The most common way to evaluate the spatial accuracy of a 3D model developed with photogrammetry is by comparing the modeled locations of control points and check points. Agisoft performs a calculation of the model's error at each control and check point in the easting (X), northing (Y), and vertical (Z) directions. The errors associated with the GCP model are shown in Tables 2 and 3.

Table 2. Errors of GCP model control points

Point #	X error (in)	Y error (in)	XY error (in)	Z error (in)	Total (in)
1	0.053	0.342	0.346	-0.746	0.822
2	0.196	0.054	0.203	-0.613	0.646
3	-0.062	0.189	0.199	-0.110	0.227
4	-0.203	-0.523	0.561	0.332	0.652
6	0.576	0.021	0.576	-0.912	1.079
7	0.044	0.257	0.261	1.565	1.586
8	-0.179	0.078	0.195	0.572	0.604
10	-0.169	-0.190	0.254	0.835	0.873
12	-0.274	-0.197	0.338	-0.898	0.960
RMSE	0.248	0.253	0.355	0.828	0.900

Table 3. Errors of GCP model check points

Point #	X error (in)	Y error (in)	XY error (in)	Z error (in)	Total (in)
5	-0.401	0.172	0.437	-0.460	0.634
9	0.124	0.396	0.415	-0.071	0.421
11	-0.386	-0.459	0.600	0.234	0.644
RMSE	0.330	0.364	0.491	0.301	0.576

The root mean square error (RMSE) is the means by which the error at all points is summarized and is calculated using Equation 1. The total horizontal (XY) error of each point is also presented and is calculated using Equation 2.

$$RMSE = \sqrt{\frac{1}{n} * \sum_{i=1}^{n} (E_i^2)} \qquad \textbf{Equation 1}$$

Where n is the number of data points, i is the index integer which ranges from 1 to n, and E is the error.

$$E_{XY} = \sqrt{E_X^2 + E_Y^2} \qquad \textbf{Equation 2}$$

Where E is the error in the direction of the subscript.

Figure 8 provides a visual representation of the error corresponding to each control and check point. Note that manual trimming removed the areas associated with the points outside of the canal. However, the reported errors still correctly correspond to the untrimmed 3D model. The Z error is represented by the ellipse color, and the X and Y errors are represented by the ellipse shape.

In the partial orthomosaic shown in Figure 8, the ground sampling distance (GSD), which is the linear distance that one pixel covers on the ground, was 0.136 in. Note that the reported GSDs are of the orthomosaic, which was developed using all oblique and nadir imagery from the four altitudes. Therefore, the GSDs are averaged in the orthomosaic, but the GSD varied among each subset of images. The GSD of each

subset was not evaluated since all subsets were combined in this research.

Figure 8. GCP model control and check point locations and error estimates

Manciola et al. (2008) indicate that a reasonable target for mean vertical error of a dam is 0.1%. Given the relatively small nature of the canal and flume studied in this research, this level of accuracy would be very difficult to achieve. To illustrate, the vertical range of the GCPs is 123.04 in. A vertical RMSE vertical less than 0.1% would require a value of 0.123 in. for the area studied in this research. The vertical RMSE associated with the GCP model, including all control and check points, is 0.762 in., which corresponds to a percent vertical error of 0.60%. When considering just the points within the canal, the vertical RMSE is reduced to 0.456 in., or a 0.37% vertical error.

The horizontal errors of the GCP model are far better than the vertical errors, which is not uncommon for photogrammetry. Considering all GCPs, the horizontal RMSE is 0.393 in., or 0.02% error relative to the maximum horizontal distance between any two GCPs, which was 1595.01 in. Similarly, the horizontal RMSE of just the points within the canal was 0.353 in., or 0.02% error.

The RTK-GPS uncertainty and the RMSEs of the photogrammetry process can be summed to provide a total uncertainty of the GCPs within photogrammetry models. Given a maximum RTK-GPS vertical uncertainty of 2 in. and horizontal uncertainty 1 in. and, the combined uncertainty of all GCPs within the GCP model was 2.762 in. vertically and 1.393 in. horizontally. The combined uncertainty of the GCPs within the canal was 2.456 in. vertically and 1.353 in. horizontally.

It is important to note that the overall accuracy demonstrated by the GCPs does not necessarily capture the accuracy of smaller features within the system that have a significant hydraulic impact, such as rocks and vegetation within the canal. As discussed in Chapter IV, the vegetation was simplified and smoothed to reduce the computational cost of each CFD simulation. The overall effect of smoothing the vegetation is outside of the scope of this research but may be an important limitation to this research. The digital rendering of the rocks, however, qualitatively appears representative of the actual canal condition.

Another important detail that photogrammetry captures is the shape of the flume itself. Upon physical inspection, it is apparent that the ramps and sill of the flume are not planar, and that the sill is not level. Figure 9 shows the upstream ramp and top of the sill. Note the non-linear ramp and sill faces indicated by the junction of the left wall with the

ramp and sill. There is no clear break in grade as the ramp transitions to the flume, and the sill itself has a slight curvature. Figure 10 shows the digital elevation model (DEM) from the GCP model with contour lines every 0.05 ft of elevation. The varying elevation on the sill and the non-parallel contours on the ramps indicate that the photogrammetry captured the unevenness of the flume.

Figure 9. Upstream ramp and sill of the LHPS flume

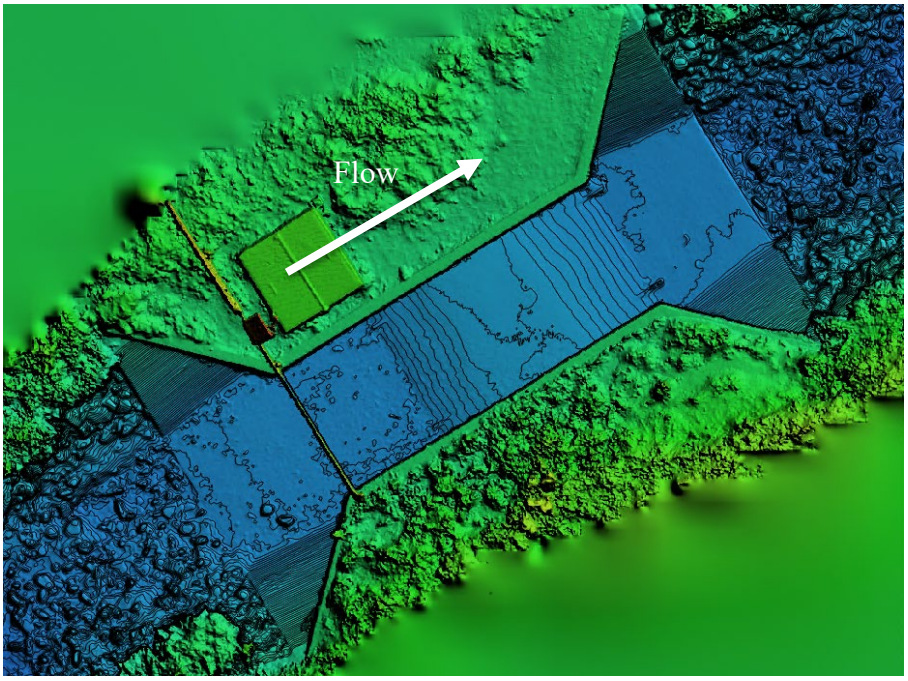

Figure 10. Digital elevation model of GCP model flume

Non-GCP Model Photogrammetry Results and Discussion

The results of the Non-GCP model are presented similarly to the GCP model. Table 4 shows the errors associated with the Non-GCP model. Figure 11 shows a visual representation of the error corresponding to check point. Again, manual trimming removed the areas associated with the points outside of the canal, but the reported errors still correctly correspond to the untrimmed 3D model. The Z error is represented by the ellipse color, and the X and Y errors are represented by the ellipse shape. In the partial orthomosaic shown in Figure 11, the GSD was 0.124 in. Figure 12 shows the Non-GCP DEM with contours every 0.05 ft. The Non-GCP DEM also appears to have captured the non-planar nature of the sill and ramps of the flume.

Table 4. Errors of Non-GCP model check points

Point #	X error (in)	Y error (in)	XY error (in)	Z error (in)	Total (in)
1	-55.250	14.727	57.179	661.949	664.414
2	-56.358	12.525	57.733	662.225	664.736
3	-55.040	7.205	55.509	663.989	666.305
4	-59.443	16.798	61.771	661.831	664.708
5	-60.096	21.297	63.758	660.959	664.027
6	-55.252	23.083	59.880	662.426	665.128
7	-51.400	5.073	51.650	666.782	668.780
8	-60.102	24.989	65.090	662.284	665.474
9	-52.828	13.261	54.467	664.518	666.746
10	-62.923	19.287	65.813	658.921	662.200
11	-60.291	9.175	60.985	658.595	661.412
12	-59.583	2.923	59.654	659.063	661.757
RMSE	57.479	15.772	59.603	661.966	664.644

Figure 11. Non-GCP model check point locations and error estimates

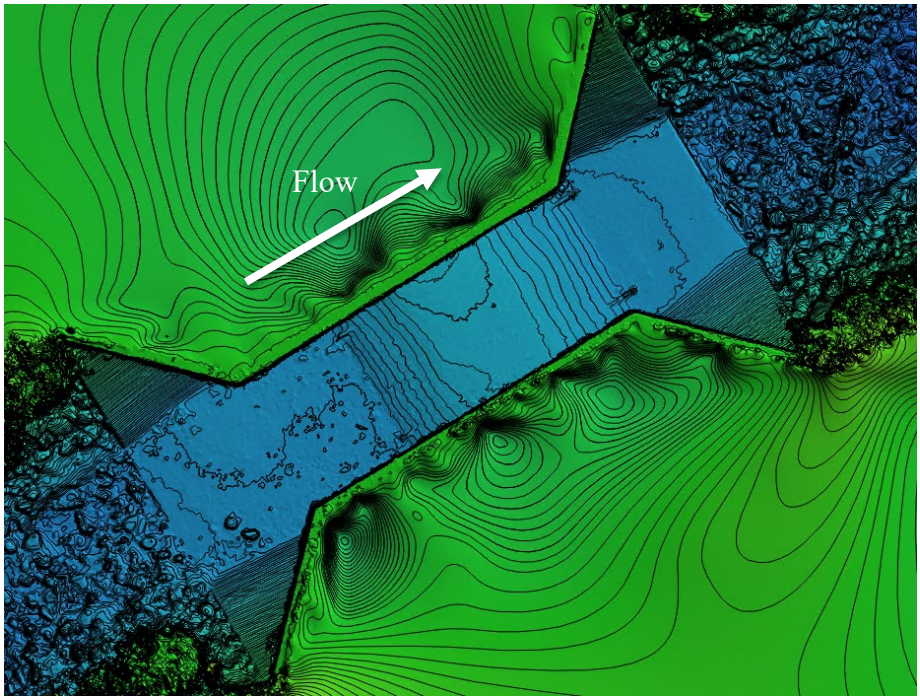

Figure 12. Digital elevation model of Non-GCP model flume

While it is common practice to use GCPs when using photogrammetry, the Non-GCP model was developed to investigate the effect of not using GCPs on the hydraulic accuracy of the model. Still the same, the spatial accuracy provides valuable context for the hydraulic accuracy.

Before discussing the accuracy of the Non-GCP model, however, it is important to discuss the difference between bias and precision, both of which contribute to overall accuracy. Bias is essentially a shift from the true value to the estimated value in the data. Precision is how similar the estimated values of the data points are to each other. The relationship between bias and precision is demonstrated in Figure 13.

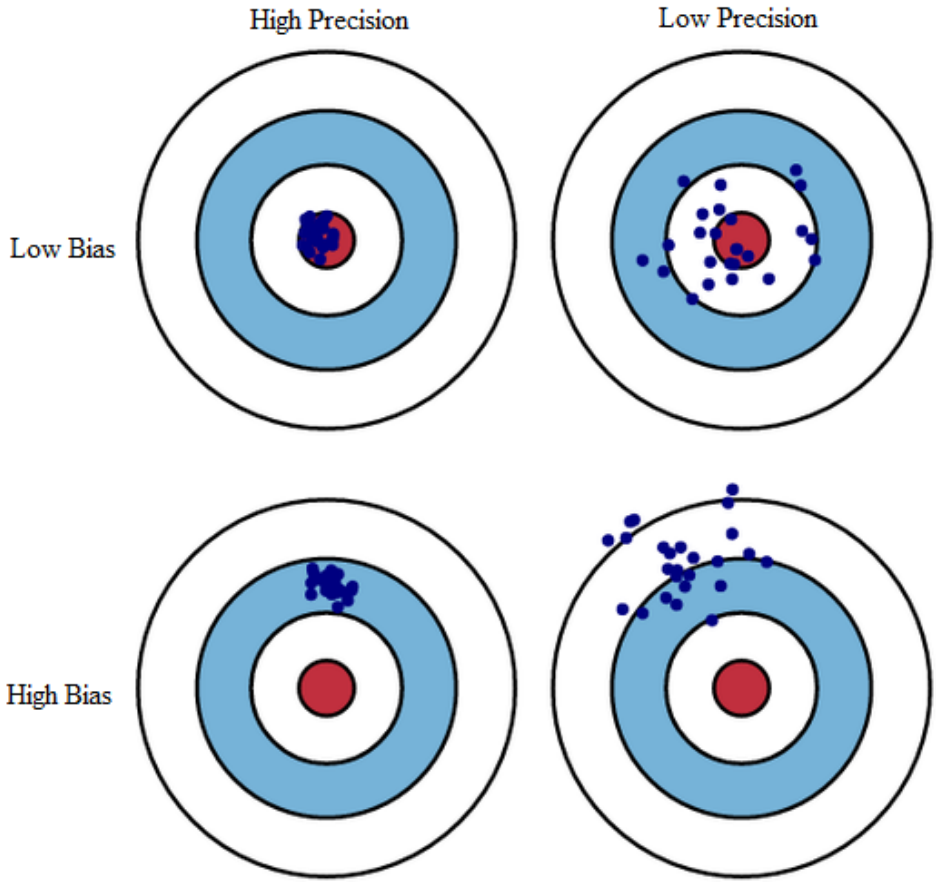

Figure 13. Illustration of the relationship between bias and accuracy (Jun 13, 2018 posting by V Singh to https://www.quora.com/What-is-bias-and-variance, unreferenced)

The ellipses in Figure 11 and data in Table 4 demonstrate that aside from the imprecision of the Non-GCP model, there is a noticeable bias in the data. The bias was likely introduced when the UAV's GPS data corresponding to each image was used within Agisoft as an initial reference for the model. The UAV's GPS data is not highly accurate, which is why it was not used for the GCP model. However, in order to provide some spatial reference, the UAV GPS data needed to be used.

In order to provide a sense of the precision of the Non-GCP model, the data presented in Table 4 was modified with a common shift in the northing, easting, and vertical directions. GCP 2 was selected as the datum for the shift since it is at the center of the study area. Accordingly, all points were respectively shifted by 56.358 in., -12.525 in., and -662.225 in. in the easting, northing, and vertical directions. The modified data is presented in Table 5.

Table 5. Modified errors of Non-GCP model check points

Point #	X error (in)	Y error (in)	XY error (in)	Z error (in)	Total (in)
1	1.108	2.202	0.554	-0.276	0.619
2	0.000	0.000	0.000	0.000	0.000
3	1.318	-5.320	2.224	1.764	2.838
4	-3.085	4.274	4.038	-0.394	4.057
5	-3.738	8.773	6.025	-1.266	6.157
6	1.107	10.559	2.147	0.202	2.156
7	4.958	-7.452	6.083	4.558	7.601
8	-3.744	12.464	7.357	0.059	7.357
9	3.530	0.736	3.266	2.293	3.991
10	-6.565	6.762	8.080	-3.304	8.729
11	-3.933	-3.350	3.252	-3.630	4.874
12	-3.224	-9.601	1.921	-3.162	3.700
RMSE	4.369	7.811	5.373	2.805	6.061

This shift does not mean that point 2 actually has zero error. Rather, it is a way to artificially remove the bias to better understand the precision of the Non-GCP model.

Therefore, instead of referring to the horizontal and vertical results in terms of accuracy, the rest of this section will use the term precision. The percent precision is once again relative to the maximum vertical and horizontal differences between GCPs, which are, respectively, 123.04 in. and 1595.01 in.

The vertical RMSE precision of all GCPs was 2.805 in, or 2.28% precision. The GCPs within the canal had a vertical RMSE precision of 0.987 in., or 0.8% precision. The horizontal RMSE of all GCPs was 5.373 in. (0.34% precision), and the RMSE precision of canal GCPs was 4.726 in. (0.30%). It is interesting that the magnitude of vertical RMSE precision was less than horizontal RMSE precision for the Non-GCP model.

The RTK-GPS uncertainty and the RMSEs of the photogrammetry process were also summed to provide a total uncertainty of the GCPs within the non-GCP model. Given a maximum RTK-GPS vertical uncertainty of 2 in. and horizontal uncertainty 1 in. and, the combined uncertainty of all GCPs within the GCP model was 4.805 in. vertically and 6.373 in. horizontally. The combined uncertainty of the GCPs within the canal was 2.987 in. vertically and 5.726 in. horizontally. These uncertainties use the modified precision of the model.

There is a significant difference between the accuracy and precision of the GCP Non-GCP models. There is approximately an order of magnitude difference between the accuracy of the GCP model and the precision of the Non-GCP model. The exception to this difference is the vertical precision of the GCPs within the canal. The GCP model's accuracy is approximately two times better than the Non-GCP model's precision.

While the spatial accuracy of the models provides valuable insight into the validity of the photogrammetry process, it may not, on its own, predict the hydraulic

accuracy of the model. The subsequent CFD analyses conducted on the various 3D models provide further insight into the effect that the absence of GCPs has on the hydraulic performance of the Non-GCP models.

GCP Model and Non-GCP Model Comparison

The GCP and Non-GCP models can also be compared qualitatively by comparing their appearance and size by overlaying them on each other. Note that this is not an inherently quantitative method to evaluate the spatial accuracy of the models, but can provide a valuable sense of the relative differences between the models. Figures 14 and 15 show the two models aligned using the upstream left corner (as looking downstream) and left wall of the flume to align the two models.

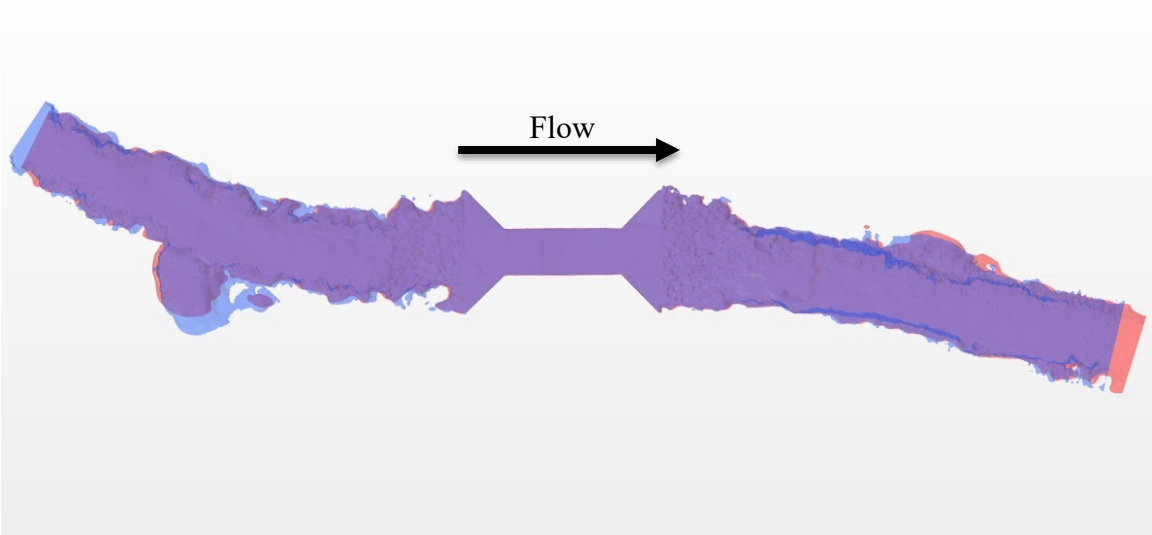

Figure 14. Plan view of overlapping GCP (red) and Non-GCP (blue) models

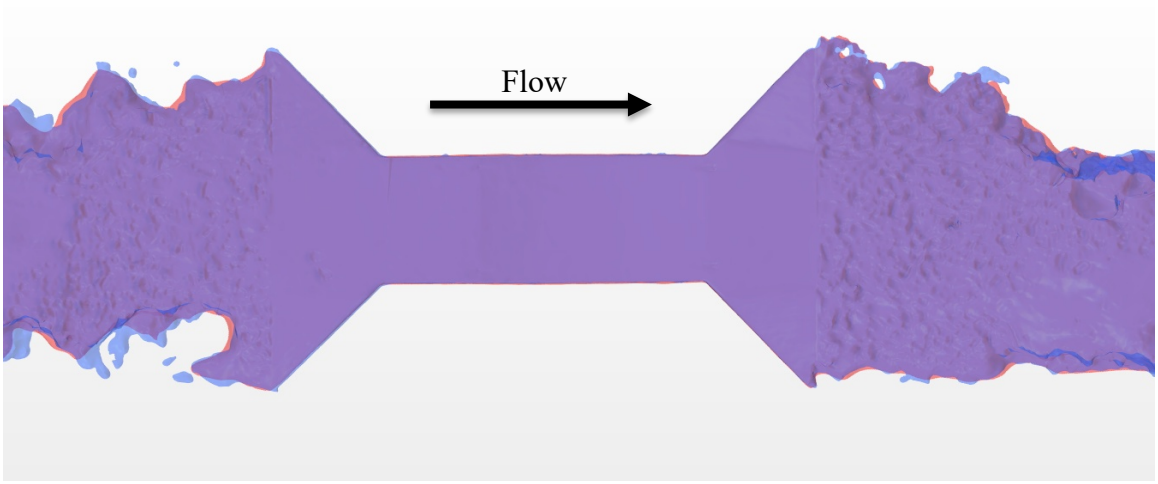

Figure 15. Plan view of overlapping GCP (red) and Non-GCP (blue) models at the flume

The spatial differences between the models are visibly apparent when considering the overlay of the two models shown in Figures 14 and 15. Most notably, the Non-GCP model is somewhat compressed compared to the GCP model. There are specific features along the bank on either the upstream or downstream ends that are closer to the flume in the Non-GCP model. There was not a noticeable difference in the vertical position of features within the canal.

CHAPTER VI

NUMERICAL MODELING

Numerical modeling with CFD was the means by which the hydraulic accuracy of the four 3D models of the LHPS flume was analyzed. The author used the CFD software package STAR-CCM+ version 14.06.013 for all simulations in this research. This chapter contains a summary of the various numerical models used in the CFD, the method used to resolve the mesh, and the results that were extracted from each simulation.

CFD Simulations

Sixteen CFD simulations were performed for this research. As discussed, four 3D models were developed to test with CFD: GCP model, Non-GCP model, As-Designed model, and As-Built model. Each model was tested at four flowrates: 10.0 cfs, 23.0 cfs, 39.7 cfs, and 50.0 cfs. The middle flowrates, 23.0 cfs and 39.7 cfs, were selected because the author visited the site and gathered imagery of the flume at these two flow rates. The outer flowrates, 10.0 cfs and 50.0 cfs, were selected because they correspond to extreme expected flowrates within the canal.

Numerical Model Setup

Since the flow within the canal is open to the atmosphere, the implicit unsteady Eulerian multiphase volume-of-fluid (VOF) model was selected to describe the materials and their interactions over time in the numerical models. The Reynolds-Averaged Navier Stokes (RANS) Equations, realizable K-Epsilon two-layer, and two-layer all y+ wall treatment models were the turbulence models used in all simulations. These models correspond with the suggested selection in the STAR-CCM+ tutorial section of the user

manual for a gravity-driven VOF flow (Accessed Mar 18, 2020).

Since the photogrammetry captured features such as pebbles and rocks within the canal, all surfaces were assumed to be smooth. Assigning roughness values to surfaces would have been redundant since the roughness was assumed to be adequately captured within the photogrammetry models.

The models and equations are solved for a volumetric domain that is defined by a mesh, or network of cells. The meshes in all simulations consisted of hexahedral (cubic) cells in Cartesian coordinates. The Cartesian coordinates were aligned such that the x direction was approximately normal to the flume walls, the y direction was parallel to the flume walls, and the z direction was vertical.

Three volumetric controls were established to increase the definition of the mesh at locations of interest. An anisotropic control was placed to envelop the air-water interface upstream and downstream of the flume. The anisotropy was set such that the horizontal (x and y) dimensions of the cells did not change from the base cell size and the vertical (z) dimension was decreased to 10% of the base size. There was also a control set for the length of the flume which uniformly decreased the cell size by 50%. A third control volume decreased the cells to 25% of the base size that extended from near the downstream end of the flume sill to about 15 ft beyond the edge of the flume.

Result Extraction

The accuracy of the CFD data is measured by comparing it to the current rating curve for the flume. The flume uses a stilling well, location shown in figure A3, to measure h_p. The h_p in the CFD simulations was measured by recording the water surface elevation. The water surface elevation was measured using an isosurface where the VOF

was 0.5 (where the composition of the cell is 50% water and 50% air) and was limited to a 1-ft diameter semicircular region. The location of the stilling well was the center of the semicircular region. The average elevation of the isosurface was recorded for the duration of the simulation. The author tested other methods to evaluate and record the time-averaged water surface elevation including a pressure probe and line probe located at the stilling well. However, the isosurface method provided the most consistent results.

Once the mass flowrate in and out of the model had become stable and nearly equal, the simulation was allowed to run for at least 30 more simulated seconds to ensure equilibrium had been reached. The average isosurface elevation was then tabulated, and the values after the system reached equilibrium were extracted and averaged to provide a single water surface elevation.

Grid Convergence

There is a degree of uncertainty associated with CFD due to the finite cells a simulation uses to describe flow through a volume. Generally speaking, the smaller the mesh, or grid, is, the less uncertainty is associated with the discrete representation of the system. Therefore, if the same simulation is performed with several different mesh sizes, the smaller meshes should provide a solution with less uncertainty. However, there is a point at which decreasing the grid size does not lead to a significantly different solution.

The Journal of Fluids Engineering's "Procedure for Estimation and Reporting of Uncertainty Due to Discretization in CFD Applications" (ASME 2008) provides guidance to evaluate the uncertainty associated with the grid size. Since all simulations at all flowrates are relatively similar, this method was only applied to one 3D model (GCP model) at one flowrate (23.0 cfs). The discretization error of the water surface elevation

measurement was 0.55%. The physical measurement device used at the flume, a float-operated recorder, has an uncertainty of 0.016 ft (USBR 2001). This uncertainty corresponds to 1.1%, 1.3%, 1.8%, and 2.9% for the 50.0 cfs, 39.7 cfs, 23.0 cfs, and 10.0 cfs simulations, respectively. Furthermore, the uncertainty of long-throated flumes is ±2% (USBR 2001). Therefore, the grid-related uncertainty of 0.55% was deemed acceptable for this research.

CHAPTER VII

NUMERICAL MODELING RESULTS AND DISCUSSION

The primary goal of this research is to evaluate the hydraulic accuracy of 3D models developed using photogrammetry. The results from the numerical models are evaluated and compared to the rating curve used by the canal company to measure the flowrate in the canal. A rating curve is the relationship between the measured water level and the flowrate, or discharge, in the canal. The first comparison addresses the relative difference between the current rating curve and the numerical model h_p results at the four modeled flowrates (10.0 cfs, 23.0 cfs, 39.7 cfs, 50.0 cfs). The second comparison involves the development of a rating curve from each of the four 3D models' CFD results and comparing them to the current rating curve.

The rating curve for the LHPS flume was established by the civil engineering company that designed the flume using WinFlume version 1.06.0002. WinFlume is a software developed and provided to the public by the United States Bureau of Reclamation, Agricultural Research Service, and International Institute for Land Reclamation and Improvement. The software is widely used by practicing engineers to design and calibrate long-throated flumes and broad-crested weirs. Note that the rating curve is established theoretically within WinFlume and has not been verified by field calculations. Table A1 presents the WinFlume output rating table from the LHPS flume.

Relative Differences Between Piezometric Head Readings

The results from the CFD simulations, shown in Table 6, are presented by comparing the rating curve's predicted h_p at a given flowrate to the corresponding h_p acquired from the CFD simulations.

Table 6. CFD piezometric head results compared to rating curve piezometric heads

Model	Flowrate (cfs)	Rating Curve h_p (ft)	CFD h_p (ft)	Total Difference (ft)	% Difference
GCP	10.0	0.548	0.593	0.045	7.63%
	23.0	0.913	0.928	0.015	1.67%
	39.7	1.274	1.250	-0.025	-1.96%
	50.0	1.467	1.413	-0.053	-3.78%
Non-GCP	10.0	0.548	0.603	0.055	9.15%
	23.0	0.913	0.906	-0.007	-0.75%
	39.7	1.274	1.251	-0.024	-1.88%
	50.0	1.467	1.441	-0.025	-1.76%
As-Designed	10.0	0.548	0.629	0.081	12.94%
	23.0	0.913	0.972	0.059	6.09%
	39.7	1.274	1.285	0.011	0.83%
	50.0	1.467	1.473	0.006	0.42%
As-Built	10.0	0.548	0.595	0.047	7.88%
	23.0	0.913	0.981	0.068	6.96%
	39.7	1.274	1.300	0.026	2.02%
	50.0	1.467	1.498	0.031	2.07%

The accuracy of the CFD simulations is expressed as the total difference (see Figure 16) and percent difference (See Figure 17) between each CFD simulation's h_p and the rating curve's h_p at each flowrate numerically modeled. The total difference is calculated by subtracting the rating curve's h_p from the CFD simulation's h_p. The percent difference is calculated using Equation 3. The two difference types are considered since the percent difference is increasingly sensitive to small total differences at low flowrates. For example, the As-Built model reported a percent difference of 7.88% at 10.0 cfs and 6.96% at 23.0 cfs. However, the total differences at 10.0 cfs and 23.0 cfs were, respectively, 0.047 ft and 0.068 ft. Thus, we see that while percent difference is generally an appropriate method to compare results, there may be some details that are lost due to the percent difference's sensitivity at low flowrates. In addition to comparing the numerical model results solely to each other, the actual h_p readings for each CFD

simulation are compared to the rating curve in Figure 18.

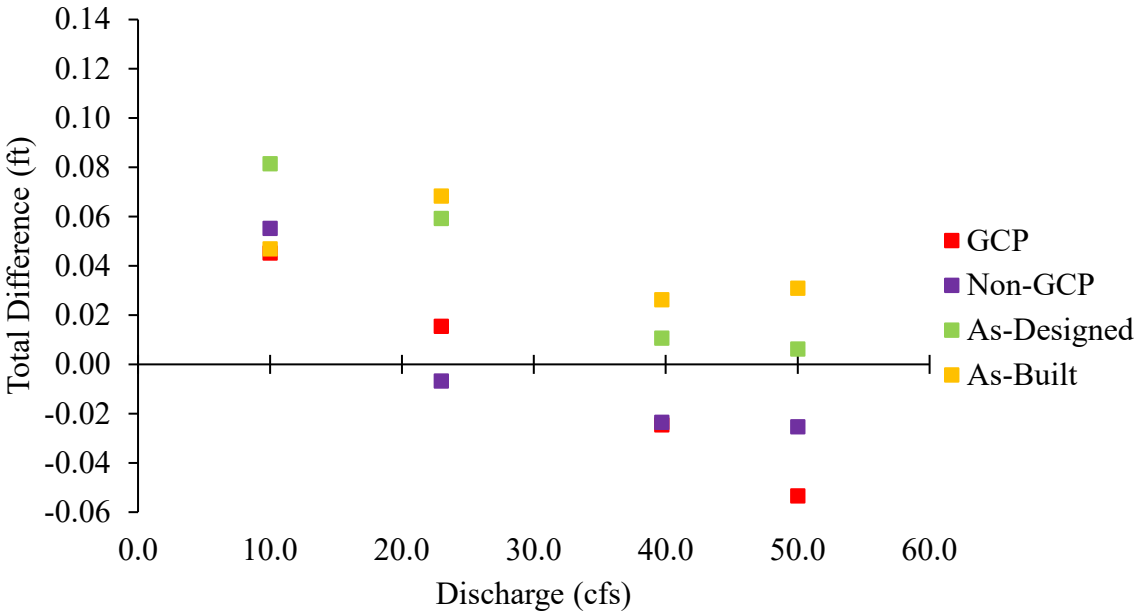

Figure 16. Total piezometric head difference of numerical model results

$$\%\ Diff = \frac{h_{p-CFD} - h_{p-RC}}{h_{p-RC}} * 100\% \qquad \textbf{Equation 3}$$

Where h_p is the piezometric head, the *CFD* subscript denotes the CFD result, and the *RC* subscript denotes the rating curve value.

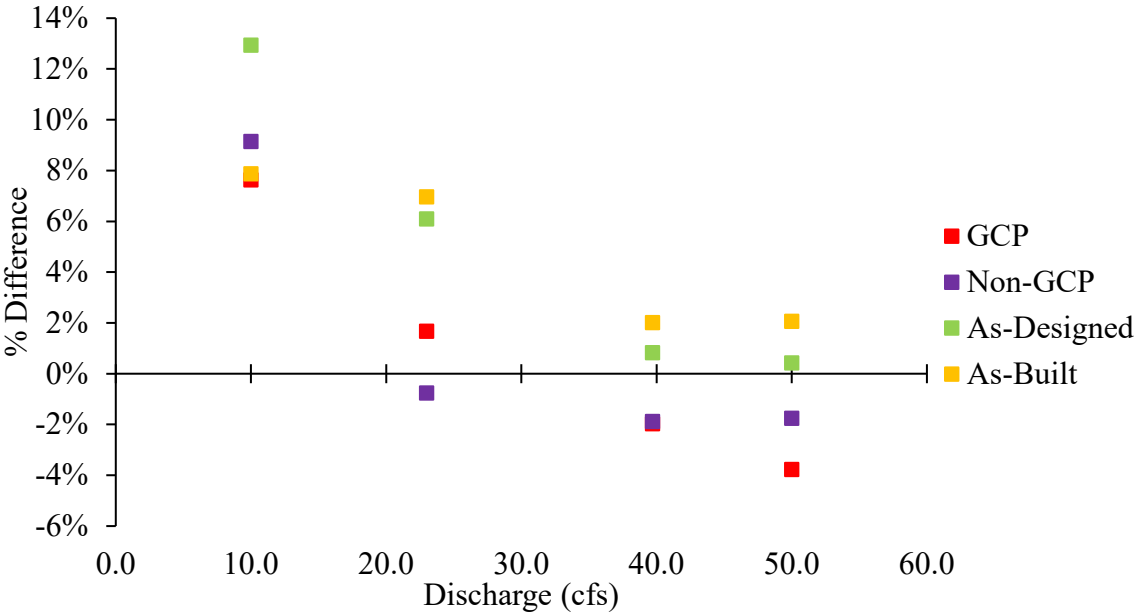

Figure 17. Percent piezometric head difference of numerical model results

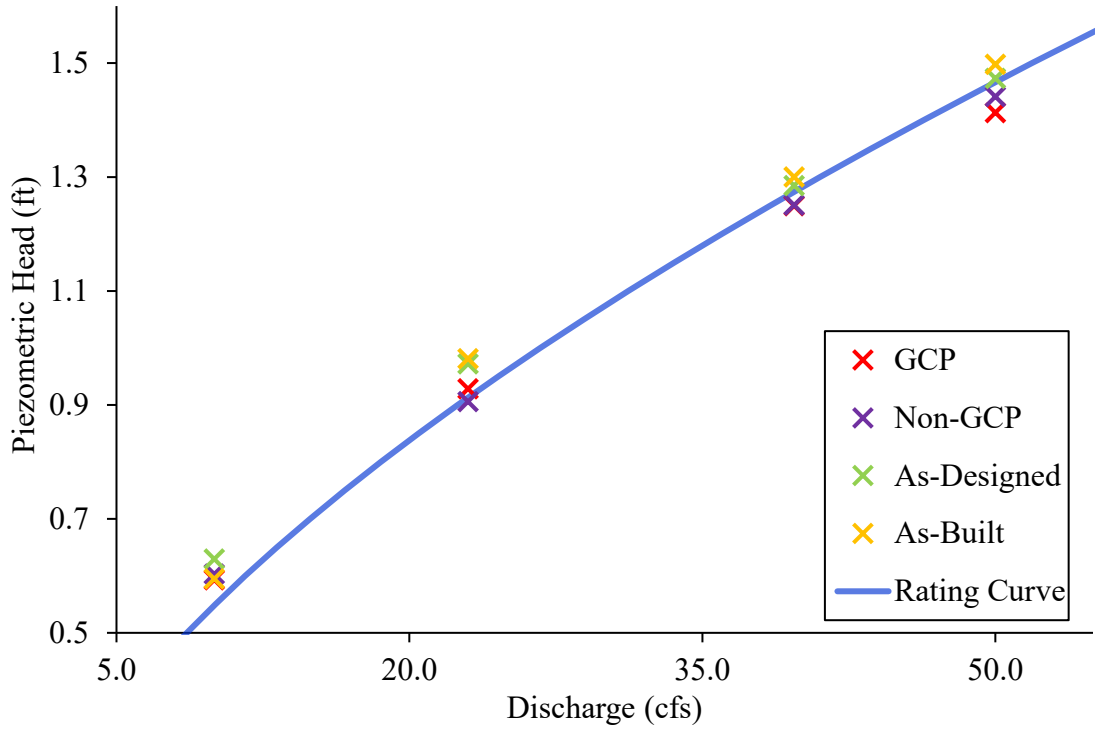

Figure 18. CFD piezometric head readings compared to rating curve

Based on these results, it appears that each model type shares the general trend of differences decreasing as flowrates increase. All four models had the highest percent difference of their respective results at 10.0 cfs. Note that the Non-GCP model had smaller total and percent differences for all flowrates, except for 10.0 cfs, than the GCP model. However, there doesn't appear to be as clear of a trend among the Non-GCP data, which could indicate uncertainty associated with the differences in geometry discussed in Chapter VI. The GCP model also seems to have decreased accuracy as flowrates move beyond 50.0 cfs.

Numerical Model Rating Curves

Although Figures 16, 17, and 18 provide a valuable sense of the numerical models' respective differences, a rating curve was established for each 3D model's CFD

results. The rating curves are of the same form used by WinFlume, which is shown in Equation 4. Developing a rating curve for each dataset improves the understanding of the hydraulic performance of each 3D model.

$$Q = K_1 * (h_p + K_2)^u \qquad \textbf{Equation 4}$$

Where Q is a flowrate in cfs, K_1 and u are constants, and K_2 is a head offset constant in ft.

The three constants were determined using the GRG Nonlinear solver using central derivatives within Microsoft Excel. The resulting rating curves are shown in Figure 19. Figure 19 also features the normal operating condition bounds for the canal of 35 and 45 cfs (2020 SMS text message from J Morgado to the author). Figure 20 then focuses on the rating curves within the normal operating flowrates and includes the bounds associated with the 2% uncertainty of long-throated flumes (USBR 2001).

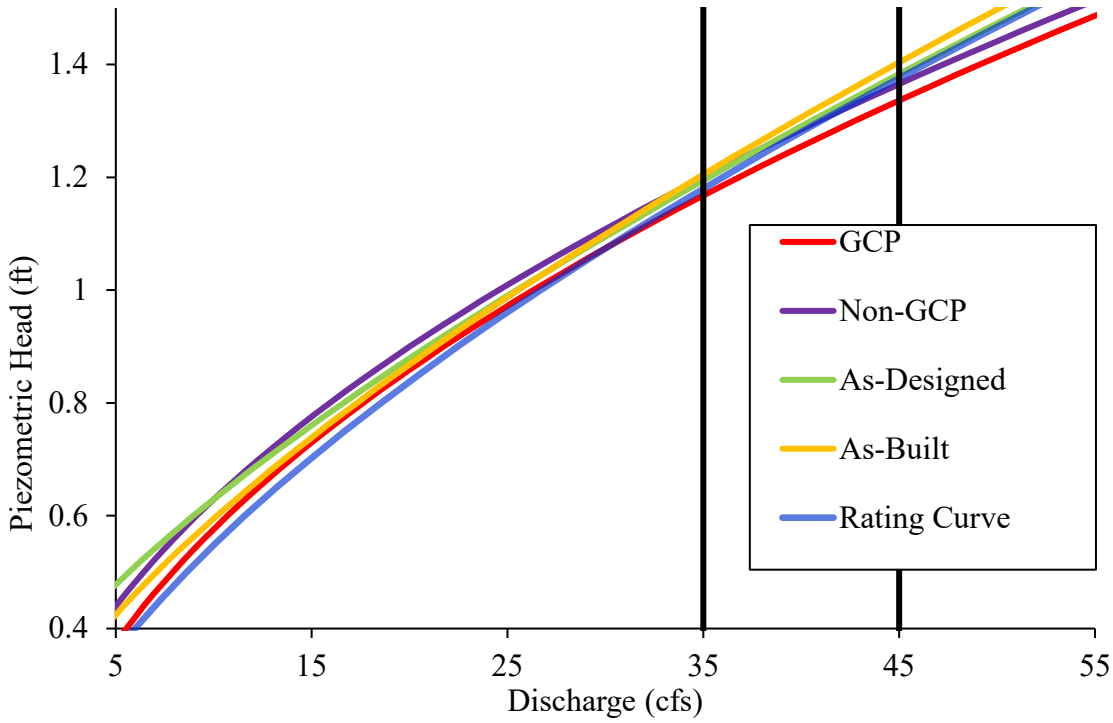

Figure 19. Existing rating curve and numerical model result-based rating curves

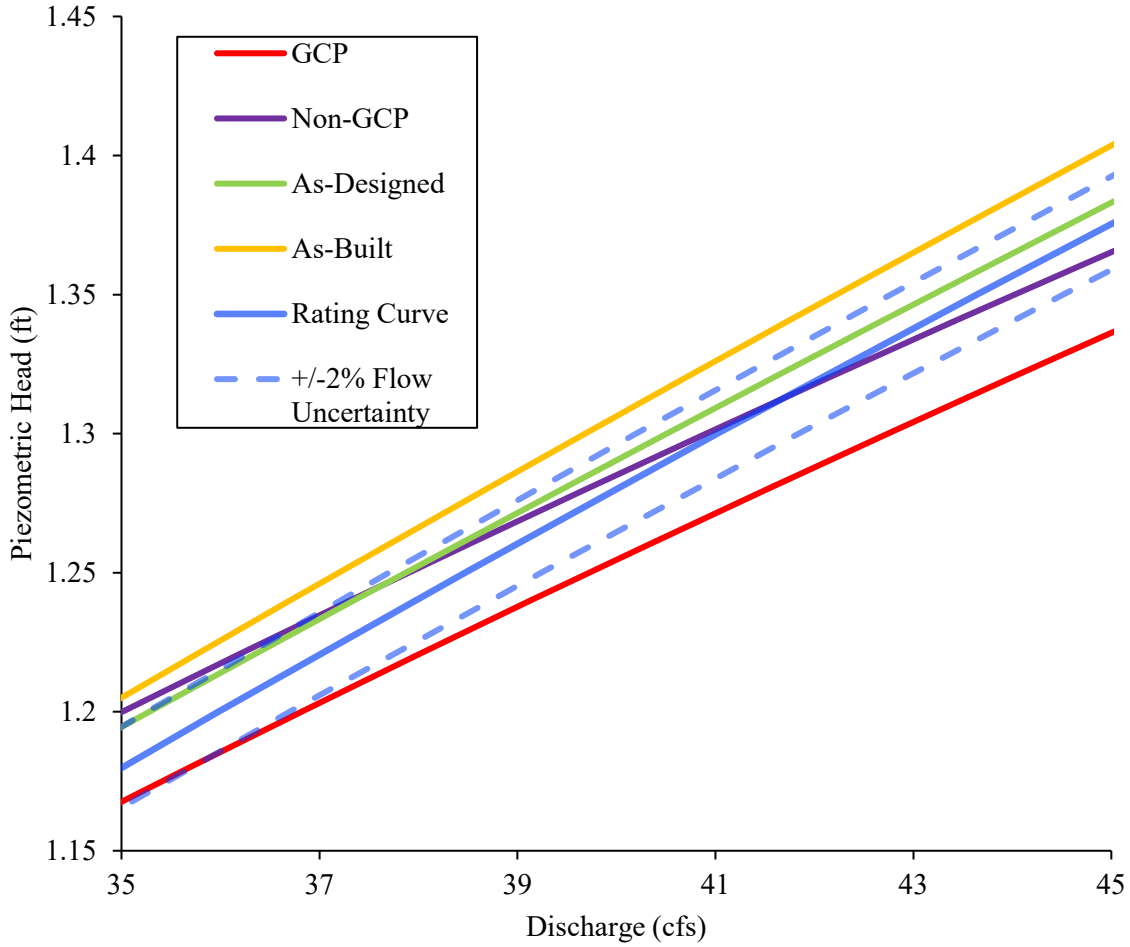

Figure 20. Existing rating curve and numerical model result-based rating curves within normal operating flowrates

Examination of Figure 19 indicates that at low flowrates, the GCP model's rating curve matches the existing rating curve closer than any other model. However, once the flowrate is within the normal operating range, the As-Designed model's rating curve matches the existing rating curve more closely.

Additionally, the As-Designed hybrid model may be considered the most geometrically similar model to the flume analyzed within WinFlume. The general shape of the As-Designed rating curve is certainly the most similar to the existing rating curve. Although the numerical model results at low flowrates show high difference, the As-

Designed curve approaches the actual curve as flowrate increases. Within the normal operating range, the As-Designed model is the curve most similar to the existing rating curve, which indicates at least a moderate correlation between the two curves.

Given the similarity between the As-Designed rating curve and existing rating curve, it stands to reason that the GCP rating curve may actually offer a more correct calibration of the flume. The As-Designed model uses the canal conditions used in the GCP model but replaces the photogrammetry-derived flume with a flume with clean geometry that matches what WinFlume analyzed to develop the existing rating curve. Since the flume itself is subject to debris gathering in or near the flume and does not actually feature clean geometry such as planar ramps and a flat, level sill, the GCP model likely captures the existing physical conditions that WinFlume and the As-Designed model are unable to. Figure 9 shows the non-planar construction of the ramp and sill and Figure 21 shows some debris and sediment that has gathered at the mouth of the flume.

Figure 21. Debris and sediment collected at the mouth of the flume

While the actual accuracy of the four experimental models is difficult to verify when compared to the existing rating curve since it is also theoretical, important conclusions can be drawn when comparing the CFD results to each other. For example, it is interesting to note the differences between the non-hybrid models (GCP and Non-GCP) and the hybrid models (As-Built and As-Designed). The GCP and Non-GCP rating curves have the same general shape, but the two are slightly offset at all flowrates. The shape of the two curves is quite similar, so the offset is fairly consistent, even outside of the normal operating flowrates. The As-Built and As-Designed rating curves do not match each other quite as well as the GCP and Non-GCP curves. However, the hybrid models' rating curves are more similar to each other than either the GCP or Non-GCP curves.

The hybrid models were developed to reflect former research that was discussed in Chapter II. The non-hybrid models were created in a novel way to develop 3D models of not only the channel but a hydraulic structure, as well. The CFD results indicate that the hybrid and non-hybrid models do not perform the same. The differences between the two types of models that are observed in this research likely originate from photogrammetry's ability to capture a more accurate geometry of the structure than the geometries that were used for the hybrid models.

Although the theoretical existing rating curve does not allow for a true evaluation of the accuracy of the models, there is a noticeable difference between the hydraulic performance of hybrid and non-hybrid models.

CHAPTER VIII

CONCLUSION

UASs are a valuable tool that can be used to improve engineers' and scientists' ability to accurately model hydraulic structures. UASs provide a cost-effective means to efficiently collect high-quality aerial photographs of important flow structures. Those photographs can then be processed using photogrammetry to develop 3D models of flow structures.

The flow structure studied in this research was an 8 ft ramp flume constructed in an unlined canal. Two models of the flume and canal, the GCP model and Non-GCP model, were developed using the Agisoft Metashape photogrammetry software. The GCP model utilized GCPs as control points during the photogrammetry process, and the Non-GCP model did not. The GCP model had horizontal and vertical RMSEs of 0.3933 in. and 0.3724 in., respectively. The Non-GCP model had horizontal and vertical RMSEs of 59.6031 in. and 661.9658 in., respectively. When the Non-GCP data was shifted to artificially remove bias, the RMSE of horizontal and vertical precision were 5.3729 in. and 2.8054 in., respectively.

The GCP model was also used to develop two additional hybrid models, wherein the photogrammetry-derived flume was removed and replaced with one of two flumes created within Autodesk Inventor. One flume was created using the original design dimensions, and another was created using dimensions physically collected from the study site. The corresponding hybrid models are referred to as the As-Designed model and the As-Built model.

Each of the four models (GCP, Non-GCP, As-Designed, and As-Built) were

numerically modeled using the STAR-CCM+ CFD software. Each model was tested at four flowrates: 10.0 cfs, 23.0 cfs, 39.7 cfs, and 50.0 cfs. The water surface elevation at the stilling well location was recorded for all simulations to compare to the expected piezometric head from the flume's rating curve. The difference for each model at 10.0 cfs, 23.0 cfs, 39.7 cfs, and 50 cfs is, respectively:

- GCP: 0.045 ft (7.63%), 0.015 ft (1.67 %), -0.024 ft (-1.96%), and -0.053 ft (-3.78%)
- Non-GCP: 0.055 ft (9.15%), -0.007 ft (-0.75%), -0.024 ft (-1.88%), -0.025 ft, (-1.76%)
- As-Designed: 0.081 ft (12.94%), 0.059 (6.09%), 0.011 ft (0.83%), 0.006 ft (0.42%)
- As-Built: 0.047 ft (7.88%), 0.068 ft (6.96%), 0.026 ft (2.02%), and 0.031 ft (2.07%)

None of the models demonstrated low differences from the existing rating curve at all flowrates. The GCP model demonstrated the most consistent rate of change of relative difference among all flow rates. The Non-GCP and As-Built models' CFD results were more sporadic when compared to the rating curve.

When comparing the rating curves that were developed for each of the four experimental models, it was clear that the non-hybrid models' hydraulic performance was quite different from that of the hybrid models. This difference in hydraulic performance denotes that the way an existing hydraulic structure is modeled causes a noticeable impact on the results. Since the existing rating curve for the structure modeled in this research is theoretical, it is not possible to evaluate which modeling method, hybrid or

non-hybrid, is more accurate.

Potential Future Research and Practical Applications

UASs have a broad field of applications within the engineering and scientific community. This research has investigated a novel combination of aerial imagery, photogrammetry, and numerical modeling with CFD. The results indicate that this combination of technologies provides an accurate method to assess a flow structure's performance. Further research can strengthen and improve the workflow discussed in this thesis.

The method in which vegetation along the banks can be accurately modeled should be investigated. The greatest uncertainty within the numerical modeling can likely be attributed to smoothing the vegetation into a solid surface. That uncertainty can be identified and reduced if research is conducted to evaluate how to accurately model vegetation captured during the photogrammetry process.

One of the most interesting and perhaps beneficial topics of future research is the ability to scale this process to larger flow structures such as dams and their spillways. Photogrammetry is already being used to study the structural safety of dams (Ridolfi et al. 2017, Henriques and Roque 2015). Expanding the use of photogrammetry to monitor structural changes over time would be useful for inspection of any hydraulic structure. UAVs provide an easy, low-cost, consistent, and safe option to inspect structures. The consistency available with aerial imagery reduces the possibility of human errors associated with manual inspections.

It is also possible that photogrammetry can be implemented to develop numerical models of spillways to assist with dam safety work. As has been discussed, there are

likely differences between the true geometric form of structures and their form when they are modeled within CAD software based on design or construction drawings. Those geometric differences, as was also observed in this research, lead to noticeable differences in CFD modeling.

Prior to implementing this method in practice, though, research should also be conducted to identify how well photogrammetry captures geometric changes to flow structures that affect the structures' hydraulic performance. For example, in addition to the geometric differences already discussed, a large concrete structure may settle or sustain superficial damage over time. Such changes would likely alter the hydraulic performance of the structure. Photogrammetry and numerical modeling could be paired to develop an updated rating curve for the structure. Further research would serve to validate the use of photogrammetry for numerical modeling and establish a reliable workflow.

REFERENCES

American Society of Civil Engineers. 2018. “America’s Infrastructure Report Card 2017.” Accessed December 11, 2019. https://www.infrastructurereportcard.org/.

American Society of Civil Engineers, Utah Section. 2016. “2015 Report Card for Utah’s Infrastructure.” Accessed December 11, 2019. https://www.infrastructurereportcard.org/state-item/utah/.

Water Measurement Manual. 2001. Denver: U.S. Government Printing Office.

Aber, J.S., Marzolff, I., Ries, J.B. 2010. *Small-Format Aerial Photography: Principles, Techniques and Geoscience Applications*. Oxford (UK): Elsevier. Chapter 3, Photogrammetry; p. 23-39.

Casas, A., Benito, G., Thorndycraft, V.R., Rico, M. 2006. “The topographic data source of digital terrain models as a key element in the accuracy of hydraulic flood modeling.” Earth Surf. Process. Landf. 31:444-456.

Chao, H., Jensen, A.M., Han, Y., Chen, Y., Mckee, M. 2009. *AggieAir: Towards low-cost cooperative multispectral remote sensing using small unmanned aircraft systems*. In: Jedlovec, G. Advances in geoscience and remote sensing. London (UK): IntechOpen Limited; p. 463-490.

Chen, Y., DiBiase, R.A., McCarroll, N., Liu, X. 2019. “Quantifying flow resistance in mountain streams using computational fluid dynamics modeling over structure-from-motion photogrammetry-derived microtopography.” Earth Surf. Process. Landf. 44:1973-1987

Colomina, I., Molina, P. 2014. “Unmanned aerial systems for photogrammetry and remote sensing: A review.” ISPRS J Photogramm. Remote Sens. 92:79-97.

Cook, C.B., Richmond, M.C., Serkowski, J.A., Ebner, L.L. 2002. “Computational fluid dynamics modeling of a spillway and tailrace: case study of the Dalles project.” In *Proc., Hydrovision 2002*. Portland: US Department of Energy.

Henriques, M.J., Roque, D. 2015. Unmanned Aerial Vehicles (UAV) As a support to visual inspections of concrete dams. In *Proc., the Second Int. Dam World Conf.*, 1-12. Lisbon, Portugal.

Khaloo A, Lattanzi D, Jachimowicz A. 2018. Utilizing UAV and computer vision for visual inspection of a large gravity dam. [accessed 2020 Feb 3]. doi: 10.20944/preprints201801.0235.v1.

Loor AD, O’Mahoney T, Kortlever W. 2018. Determining flow velocities at damaged weir of grave using CFD. In: Bung D, Tullis B, editors. Hydraulic Structures 2018.

International symposium on hydraulic structures; May 15-18. Aachen, Germany: IAHR. p. 656-666.

Manciola P, di Francesco S, Biscarini C. 2008. Flood protection and risk management: the case of Tescio River basin. In: Liebscher HJ, Clarke R, Rodda J, Schultz G, Schumann A, Ubertini L, Young G, editors. Hydrology in Water Resources Management 2008. Proceedings of a symposium on the role of hydrology in water resources management; Oct; Capri, Italy. Wallingford, UK: IAHS Press. p. 178-183.

Procedure for estimation and reporting of uncertainty due to discretization in CFD applications. 2008. ASME J. Fluids Eng. 130(7): 078001

Przybilla HJ, Webster-Ebbinghaus W. 1979. Aerial photos by means of radio-controlled aircraft. [Bildflug mit ferneglenktem Kleinflugzeug.] Bildmessung Und Luftbildwesen, 47(5), p. 137-142.

Reali A. 2018. Potentialities of unmanned aerial vehicles in hydraulic modelling. Stockholm: Kth Royal Institute of Technology.

Ridolfi E, Buffi G, Venturi S, Manciola P. 2017. Accuracy analysis of a dam model from drone surveys. Sensors. 17(8):1777-1795.

Schumann G, Matgen P, Cutler MEJ, Black A, Hoffmann L, Pfister L. 2008. Comparison of remotely sensed water stages from LiDAR, topographic contours and SRTM. ISPRS J Photogramm. Remote Sens. 63(3):283-296.

Siemens PLM. Unknown date. Selecting the physics models. Plano (TX). [accessed 2020 Mar 18] file:///C:/Program%20Files/Siemens/14.06.013-R8/STAR-CCM+14.06.013-R8/doc/en/online/index.html#page/STARCCMP%2FGUID-CAE4ABD5-CF04-4542-A89B-0CBFEDF92599.html%23

Smith MW, Vericat D. 2015. From experimental plots to experimental landscapes: topography, erosion and deposition in sub-humid badlands from structure-from-motion photogrammetry. Earth Surf. Process. Landf. 40:1656-1671.

Torres G. 2019. Drone photogrammetry vs. LIDAR: what sensor to choose for a given application. [accessed 2020 Jan 13]. https://wingtra.com/drone-photogrammetry-vs-lidar/

Willeitner RP, Barfuss SL, Johnson MC. 2013. Using numerical modeling to correct flowrates for submerged Montana flumes. J Irrig. Drain. E-ASCE. 139(7): 586-592

Zeng J, Rakib Z, Ansar M, Dessalegne T, Hajimirzaie S. 2018. Applications of CFD for flow rating at complex water control structures. In: Kamojjala S, editor. World Environmental and Water Resources Congress 2018; Jun 3-8. Minneapolis, MN: EWRI, ASCE. p. 210-221

APPENDIX

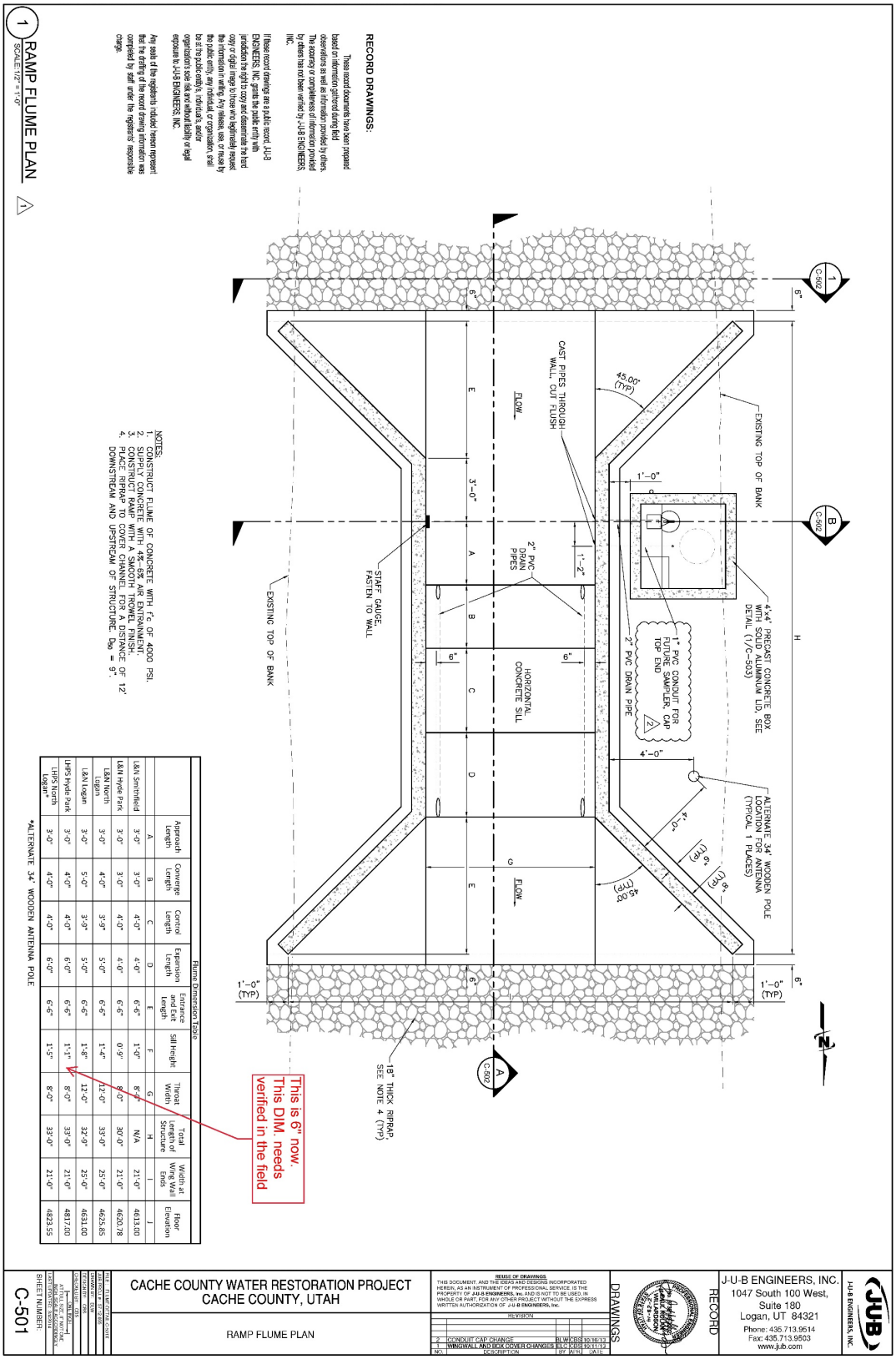

Figure A1. Plan view design drawing of LHPS flume (J-U-B Engineers 2014)

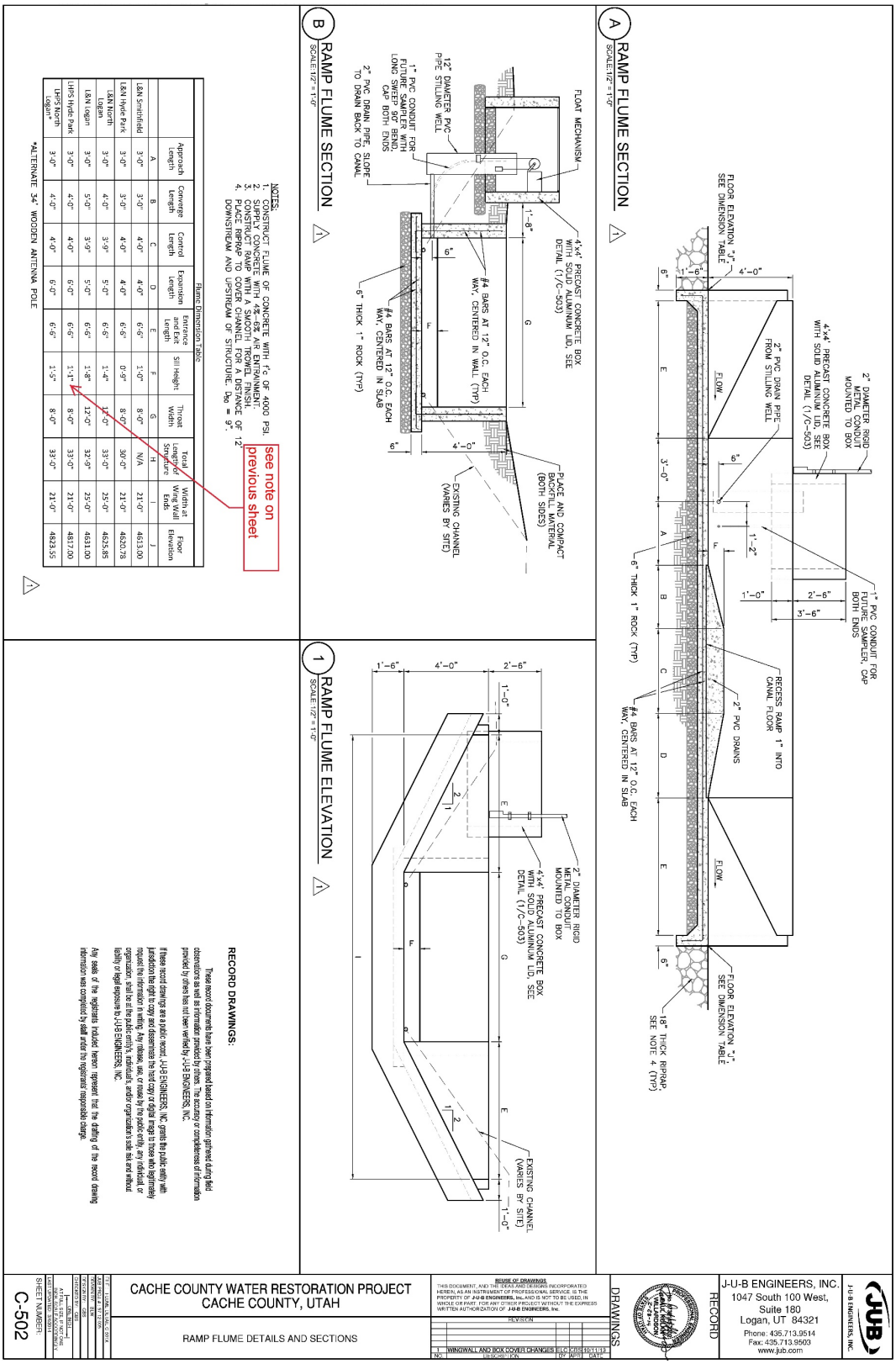

NOTES:
1. CONSTRUCT FLUME OF CONCRETE WITH f'_c OF 4000 PSI
2. SUPPLY CONCRETE WITH 4% - 6% AIR ENTRAINMENT.
3. CONSTRUCT RAMP WITH A SMOOTH TROWEL FINISH.
4. PLACE RIPRAP TO COVER CHANNEL FOR A DISTANCE OF 12' DOWNSTREAM AND UPSTREAM OF STRUCTURE. $L_{RR} = 9'$.

see note on previous sheet

Flume Dimension Table										
	Approach Length	Converge Length	Control Length	Expansion Length	Entrance and Exit Length	Sill Height	Throat Width	Length of Structure	Widths at Wing Wall Ends	Floor Elevation
	A	B	C	D	E	F	G	H	I	J
L&N Smithfield	3'-0"	3'-0"	4'-0"	4'-0"	6'-6"	1'-0"	8'-0"	N/A	21'-0"	4613.00
L&N Hyde Park	3'-0"	3'-0"	4'-0"	4'-0"	6'-6"	0'-9"	8'-0"	30'-0"	21'-0"	4630.78
L&N North Logan	3'-0"	4'-0"	5'-0"	5'-0"	6'-6"	1'-4"	12'-0"	33'-0"	25'-0"	4635.85
L&N Logan	3'-0"	5'-0"	3'-9"	5'-0"	6'-6"	1'-8"	12'-0"	32'-9"	25'-0"	4631.00
LHPS Hyde Park	3'-0"	4'-0"	4'-0"	6'-0"	6'-6"	1'-1"	8'-0"	33'-0"	21'-0"	4617.00
LHPS North Logan*	3'-0"	4'-0"	4'-0"	6'-0"	6'-6"	1'-5"	8'-0"	33'-0"	21'-0"	4623.55

*ALTERNATE 34' WOODEN ANTENNA POLE

RECORD DRAWINGS:

These record documents have been prepared based on information gathered during field observations as well as information provided by others has not been verified by J-U-B ENGINEERS, INC.

If these record drawings are a public record, J-U-B ENGINEERS, INC. grants the public entity with jurisdiction the right to copy and disseminate the hard copy or digital image to those who legitimately request the information in writing. Any release, sale, or resale by the public entity, any individual, or organization, shall be at the public entity's, individual's, and/or organization's sole risk and without liability or legal exposure to J-U-B ENGINEERS, INC.

Any seals of the registrants indicated hereon represent that the drafting of the record drawing information was completed by staff under the registrants' responsible charge.

CACHE COUNTY WATER RESTORATION PROJECT
CACHE COUNTY, UTAH

RAMP FLUME DETAILS AND SECTIONS

REVISION			
NO.	DESCRIPTION	BY	DATE
1	WINGWALL AND BOX COVER CHANGES	ELC	10/11/19

RECORD DRAWINGS

J-U-B ENGINEERS, INC.
1047 South 100 West, Suite 180
Logan, UT 84321
Phone: 435.713.9514
Fax: 435.713.9503
www.jub.com

PROJECT MGR.	ELC
DESIGNED	GEB
DRAWN	JLW
CHECKED	ELC
QA/QC	ELC
APPROVED	ELC

SHEET NUMBER: C-502

Figure A2. Profile and cross-section design drawing of LHPS flume (J-U-B Engineers

2014)

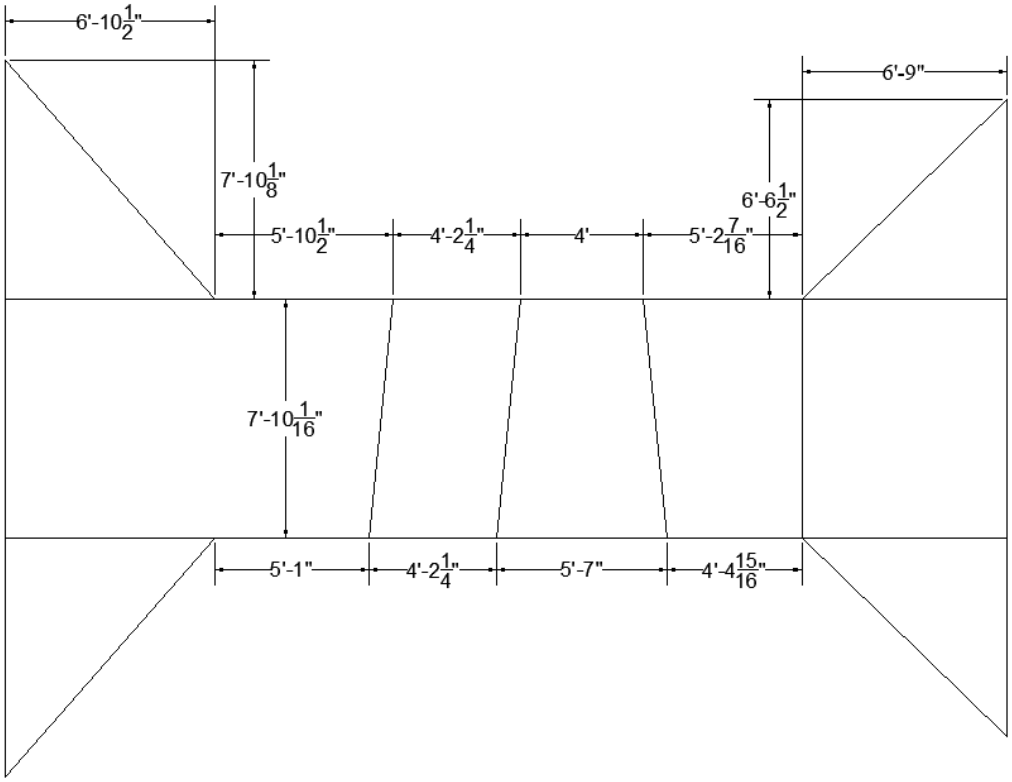

Figure A3. Plan view drawing of LHPS flume with measured actual dimensions

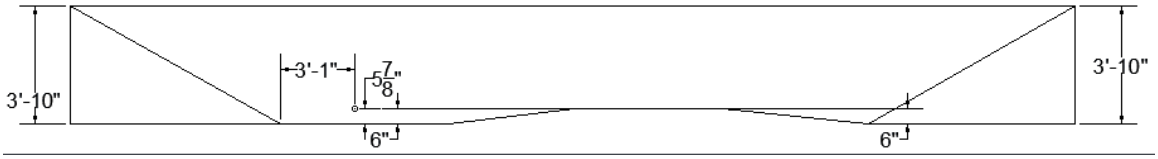

Figure A4. Profile view drawing of LHPS flume with measured actual dimensions

Table A1. WinFlume rating table for LHPS flume

Head at Gage, h1 feet	Discharge cfs	Froude Number	Required Head Loss ft	H1/L Ratio	Submerge. Ratio	Warnings
0.200	1.93	0.073	0.049	0.023	0.000	5
0.250	2.78	0.094	0.056	0.029	0.000	5
0.300	3.74	0.115	0.062	0.035	0.000	5
0.350	4.81	0.135	0.069	0.041	0.000	5
0.400	5.98	0.154	0.075	0.047	0.089	5
0.450	7.25	0.172	0.081	0.053	0.220	5
0.500	8.61	0.190	0.087	0.059	0.324	5
0.550	10.06	0.206	0.093	0.065	0.408	5
0.600	11.59	0.221	0.099	0.071	0.476	
0.650	13.21	0.236	0.105	0.077	0.533	
0.700	14.91	0.250	0.110	0.084	0.581	
0.750	16.68	0.263	0.116	0.090	0.621	
0.800	18.54	0.276	0.121	0.096	0.656	
0.850	20.47	0.288	0.127	0.103	0.686	
0.900	22.47	0.299	0.132	0.109	0.712	
0.950	24.55	0.310	0.138	0.116	0.735	
1.000	26.70	0.320	0.143	0.122	0.755	
1.050	28.92	0.330	0.149	0.129	0.773	
1.100	31.20	0.340	0.154	0.135	0.789	
1.150	33.56	0.349	0.160	0.142	0.803	
1.200	35.98	0.358	0.166	0.149	0.815	
1.250	38.47	0.366	0.171	0.155	0.827	
1.300	41.02	0.374	0.177	0.162	0.837	
1.350	43.64	0.382	0.183	0.169	0.846	
1.400	46.32	0.390	0.188	0.176	0.854	
1.450	49.07	0.397	0.194	0.182	0.861	
1.500	51.87	0.404	0.200	0.189	0.868	
1.550	54.74	0.411	0.206	0.196	0.874	
1.600	57.67	0.418	0.212	0.203	0.879	
1.650	60.65	0.424	0.217	0.210	0.884	*21
1.700	63.69	0.430	0.223	0.216	0.888	*21
1.750	66.80	0.436	0.229	0.223	0.892	*21
1.800	69.96	0.442	0.235	0.230	0.895	*21
1.850	73.17	0.448	0.242	0.237	0.899	*21
1.900	76.45	0.453	0.248	0.244	0.901	*21

Summary of Warning Messages

5 - Upstream energy head / control section length is less than 0.07.
21 - FATAL: Submergence exceeds modular limit. Critical flow will not occur.